ELSEVIER

Chemical Geology 226 (2006) 1–30

CHEMICAL GEOLOGY
INCLUDING
ISOTOPE GEOSCIENCE

www.elsevier.com/locate/chemgeo

Barium cycling in shallow sediment above active mud volcanoes in the Gulf of Mexico

D. Grace Castellini [a,b], Gerald R. Dickens [a,*], Glen T. Snyder [a], Carolyn D. Ruppel [c]

[a] *Department of Earth Sciences, Rice University, Houston, TX 77005, United States*
[b] *Kerr-McGee Oil and Gas Corporation, Houston, TX 77060, United States*
[c] *School of Earth and Atmospheric Sciences, Georgia Tech, Atlanta, GA 30332-0340, United States*

Received 16 December 2004; received in revised form 8 August 2005; accepted 17 August 2005

Abstract

Methane and other hydrocarbons fluxing upward through deep-marine sediment may strongly impact the cycling of Ba near the seafloor. Piston cores across two mud volcanoes in the northern Gulf of Mexico (GOM) were therefore examined to understand Ba cycling at regions of intense hydrocarbon gas expulsion. Pore waters were analyzed for dissolved Cl^-, SO_4^{2-} and Ba^{2+}, and sediment samples were analyzed for their extractable Ba contents. These data clearly show that saline fluids charged with hydrocarbons and dissolved Ba^{2+} (but lacking SO_4^{2-}) advect from depth and profoundly influence the Ba cycle in shallow sediment. Close to the seafloor, several processes occur over time. Usually, anaerobic oxidation of methane (AOM) and other hydrocarbons in the sediment consumes dissolved SO_4^{2-} diffusing from bottom water. As a consequence, focused CH_4 fluxing produces a sulfate–hydrocarbon transition (SHT) that shoals across the mud volcanoes. Dissolved Ba^{2+} crossing this horizon reacts with SO_4^{2-}, precipitating Ba fronts composed of barite immediately above the SHT. Smooth barite-rich carbonate nodules might form when this process remains at the same sediment horizon from extended time. Sometimes, however, venting releases dissolved Ba^{2+} into the water column, which induces barite precipitation onto the seafloor around the mud volcanoes. Episodic venting may also form and break carbonate crusts on the seafloor, producing rocky carbonate nodules cemented with barite. For both fronts and nodules, burial past the SHT leads to barite dissolution, release of dissolved Ba^{2+}, and amplification of the shallow Ba cycle.

Keywords: Barite; Marine barium cycle; Mud volcano; Gulf of Mexico; Carbonate nodule; Methane; Hydrocarbons; Sulfate; Anaerobic oxidation of methane

1. Introduction

Shallow sediments on continental slopes hold enormous quantities of low molecular weight hydrocarbons, particularly methane (CH_4), in the form of gas hydrate, free gas and dissolved gas. Collectively, these gas phases in marine sediment form open systems, with uninhibited connections to the ocean (e.g., Dickens, 2003). The abundance and distribution of gas phases in marine sediment depend on pressure, temperature, salinity, and gas concentration. Fluxes of CH_4 and other light hydrocarbons from continental slopes might, therefore, vary significantly over time in response to environmental changes (e.g., Dickens, 2003). The dynamic nature of seafloor gas systems is an outstanding issue for research, and proxies for past

* Corresponding author. Tel.: +1 713 348 5130; fax: +1 713 348 5214.
E-mail address: jerry@rice.edu (G.R. Dickens).

0009-2541/$ - see front matter © 2005 Elsevier B.V. All rights reserved.
doi:10.1016/j.chemgeo.2005.08.008

hydrocarbon outflow from marine sediment are clearly needed.

In bathyal environments, past fluxes of hydrocarbon gases might be assessed using authigenic barite ($BaSO_4$) (Dickens, 2001; Torres et al., 2003). As discussed below, gas-charged fluids in deep-marine settings generally lack dissolved sulfate (SO_4^{2-}) but contain elevated concentrations of dissolved barium (Ba^{2+}). These fluids precipitate barite when they contact SO_4^{2-} in bottom water (Fu et al., 1994; Torres et al., 1996b, 2002; Greinert et al., 2002), or in pore water of shallow sediment (Brumsack, 1986; Torres et al., 1996a; Dickens, 2001; Kasten et al., 2004; Snyder et al., in press). Authigenic barite in deep marine strata might, therefore, record past gas venting from the seafloor, or locations where hydrocarbon oxidation occurred in shallow sediment. Documentation of barite structures around modern seafloor gas vents (Fu et al., 1994; Torres et al., 1996b, 2002; Fu and Aharon, 1997; Naehr et al., 2000; Greinert et al., 2002) and barite fronts at zones of SO_4^{2-} depletion in deep-marine sediment sequences (Brumsack, 1986; Torres et al., 1996a; Dickens, 2001; Kasten et al., 2004; Snyder et al., in press) clearly support this idea. Additionally, some barite mounds and nodules that have been found in ancient deep-sea strata appear to reflect past gas expulsion (Torres et al., 2003; Clari et al., 2004). However, remarkably few studies have detailed the geochemical coupling between light hydrocarbon gases, SO_4^{2-}, and Ba in present-day seafloor sediment, especially around areas of gas venting.

The Gulf of Mexico (GOM) seems an ideal region to examine the postulated coupling. Gas hydrate and free gas have accumulated in shallow sediment at many locations (e.g., Anderson and Bryant, 1990; Brooks et al., 1990), and CH_4 and other light hydrocarbons vent at numerous mud volcanoes and seeps (e.g., Roberts et al., 1990; Neurauter and Bryant, 1990; Neurauter and Roberts, 1994; Sassen et al., 2003). Elevated Ba^{2+} concentrations occur in deep formation waters (e.g., Macpherson, 1989), and notably in interstitial waters at seeps (Fu and Aharon, 1998). Barite crusts and chimneys also have been documented on the seafloor around seeps (Fu et al., 1994; Roberts and Aharon, 1994; Fu and Aharon, 1997, 1998).

In this study, we investigate Ba cycling in shallow sediment from piston cores across two mud volcanoes in the northern GOM. Unlike most previous work conducted at other locations, both solid and dissolved constituents of Ba are examined within the context of hydrocarbon and sulfur cycling near the seafloor. The work also deviates from previous studies of Ba at vent sites in the GOM, which had only focused on the upper 40 cm of sediment in a few cores taken precisely at the location of venting (Fu et al., 1994; Fu and Aharon, 1997, 1998). Our results clearly show a strong geochemical coupling between light hydrocarbons, SO_4^{2-}, and Ba. Hydrocarbon fluxes unquestionably affect Ba cycling at these locations, although the link is more complicated than discussed for other sites (Torres et al., 1996a; Dickens, 2001; Aloisi et al., 2004; Snyder et al., in press).

2. Theoretical background

2.1. Seafloor hydrocarbon cycling

Significant amounts of organic matter reach the seafloor along many continental margins. Burial of this carbon over time induces microbially mediated reduction–oxidation (redox) reactions, which generally proceed according to free energy yield and affect the chemistry of sediment and pore water (e.g., Froelich et al., 1979; D'Hondt et al., 2004).

In areas of high organic carbon accumulation, available electron acceptors in seawater (O_2, NO_3^-, SO_4^{2-}) or sediment (MnO_2, Fe_2OOH) are readily consumed. Acetate fermentation and carbon dioxide reduction then begin converting organic matter and its intermediates to biogenic CH_4. At depth, where temperatures exceed 50 to 100 °C, thermal cracking of kerogen and bitumen generates thermogenic CH_4 and other light hydrocarbons (e.g., Tissot and Welte, 1984; Seewald, 2003). Collectively, biogenic and thermogenic sources produce high concentrations of low molecular weight hydrocarbons (particularly CH_4) in sediment along many continental margins. These elevated gas concentrations result in an upward migration of light hydrocarbons toward the seafloor, either by advection or diffusion.

For systems dominated by CH_4 and diffusion, the upward flux of hydrocarbons fuels anaerobic oxidation of methane (AOM) and consumption of SO_4^{2-} in shallow sediment (Reeburgh, 1976; Borowski et al., 1996, 1999; Hoehler et al., 2000; Boetius et al., 2000). Typically, complete removal of downward diffusing SO_4^{2-} and upward migrating CH_4 occurs across a thin (<2 m) depth interval. Although many authors have called this horizon the sulfate–methane interface (SMI) (e.g., Borowski et al., 1996), we prefer the more general sulfate–hydrocarbon transition (SHT) for two reasons. First, at a given site, SO_4^{2-} and CH_4 likely coexist and react over a depth interval rather than at a discrete point (e.g., D'Hondt et al.,

2002). Second, in some places, notably the GOM, hydrocarbons other than methane appear to consume a substantial fraction of the SO_4^{2-} (Formolo et al., 2004; Joye et al., 2004).

The SHT often lies between 10 and 40 m below seafloor (mbsf) in areas of slow CH_4 flux (Borowski et al., 1996, 1999; D'Hondt et al., 2002). In advection-dominated regimes, however, CH_4 and other light hydrocarbons can migrate rapidly along conduits to drive hydrocarbon oxidation near the seafloor and gas venting to the water column (e.g., Suess et al., 1999) (Fig. 1). This type of regime characterizes mud volcanoes and seeps in the northern GOM (e.g., Aharon and Fu, 2003; Formolo et al., 2004; Joye et al., 2004).

In theory, the upward flux of CH_4 and other hydrocarbons should dictate the rate of SO_4^{2-} consumption and the depth of the SHT (Reeburgh, 1976; Borowski et al., 1996, 1999; Hoehler et al., 2000; D'Hondt et al., 2002). Consequently, the SHT should occur close to the sediment–water interface at active mud volcanoes. Away from locations of hydrocarbon fluxing, the SHT should deepen (Fig. 1). This expectation is suggested by limited studies in the GOM (Aharon and Fu, 2000, 2003; Joye et al., 2004).

2.2. Methane–sulfate–barium coupling in shallow marine sediments

Upward fluxing hydrocarbons impact the geochemical cycling of Ba in marine sediments, particularly in deep waters. Microcrystalline barite forms in the water column when sinking organic carbon decays (Ganesham et al., 2003), and reaches the seafloor in most bathyal settings (e.g., Chow and Goldberg, 1960; Dehairs et al., 1980). Although some of this barite dissolves near the seafloor, much is buried along with other sediment (Dehairs et al., 1980). Barite dissolves when it passes through a SHT and into SO_4^{2-}-depleted, gas-rich fluids, producing high interstitial Ba^{2+} concentrations (Fig. 2). In diffusive systems, dissolved Ba^{2+} can move upwards to re-precipitate barite just above the SHT (Brumsack, 1986; Torres et al., 1996a; Dickens, 2001; Aloisi et al., 2004; Kasten et al., 2004; Snyder et al., in press). These barite fronts can record the depth of the SHT and, ultimately, constrain the flux of hydrocarbons over time (Dickens, 2001; Kasten et al., 2004; Snyder et al., in press). In areas of high fluid flux, waters rich in hydrocarbons and Ba^{2+} can discharge directly into SO_4^{2-}-rich seawater. As mentioned previously, this can lead to barite chimneys and crusts around modern seep structures (Fu et al., 1994; Torres et al., 1996b, 2002; Fu and Aharon, 1997, 1998; Naehr et al., 2000; Greinert et al., 2002; Aloisi et al., 2004) or past seep structures preserved in the geologic record (Torres et al., 2003; Clari et al., 2004).

3. Regional geology and geochemistry

The GOM is an area dominated by active salt tectonism, where structural features, bathymetry and deep formational water chemistry reflect the movement of Middle to Late Jurassic evaporite deposits

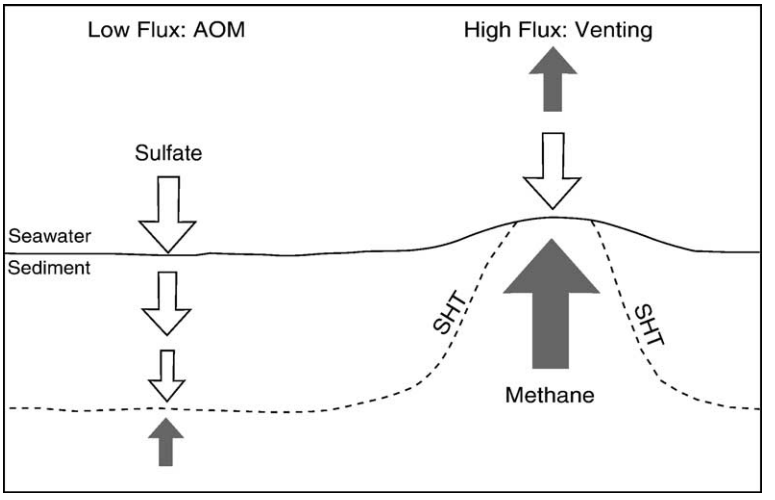

Fig. 1. The sulfate–hydrocarbon transition (SHT) across two hypothetical end-member flux regimes in marine sediment. In low flux environments, anaerobic oxidation of methane (AOM) and complete removal of pore water sulfate occurs deep below the seafloor. In high flux environments, AOM and loss of sulfate occur at or near the sediment–water interface. Active mud volcanoes should represent high flux systems.

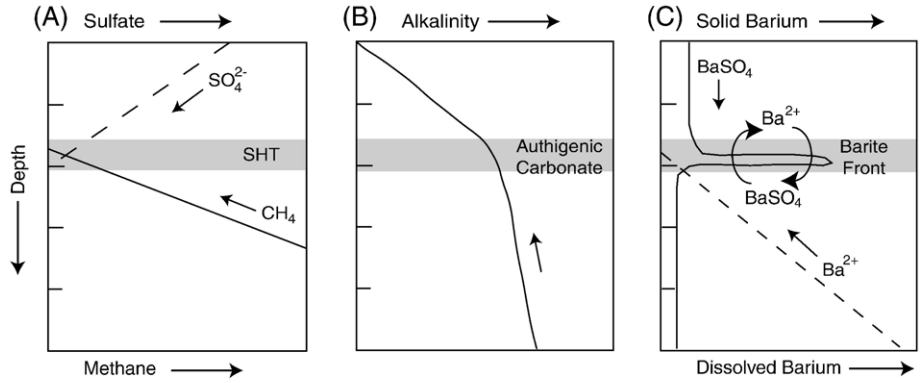

Fig. 2. Schematic profiles of pore water methane, sulfate, alkalinity and barium concentrations in shallow marine sediments above gas-rich strata (adopted from Dickens, 2001). (A) Seawater sulfate diffuses down to react with upward migrating methane across the sulfate–hydrocarbon transition (SHT). (B) Anaerobic oxidation of methane (AOM) increases alkalinity, which can lead to precipitation of authigenic carbonates that coincide with the depth of the SHT. (C) Solid barite accumulation at the surface is buried during sedimentation. As it passes through the SHT, dissolved Ba^{2+} is released. This dissolved Ba^{2+} can migrate upwards to precipitate barite in a front at the SHT.

(e.g., Worrall and Snelson, 1989). Down-slope migration of salt beginning in the late Jurassic and early Cretaceous has caused extensional faulting in the north and contractional faulting in the south (e.g., Worrall and Snelson, 1989; Peel et al., 1995; McBride, 1998). A series of structural highs and mini-basins have therefore developed between the shelf/slope break and the Sigsbee Escarpment (e.g., Deigel et al., 1995; Peel et al., 1995; McBride, 1998) (Fig. 3). The seafloor bathymetry in this region is hummocky, reflecting these underlying structural elements (e.g., Worrall and Snelson, 1989; McBride, 1998).

As salt bodies move, they create differential stress on surrounding sedimentary packages, which induces fracturing and faulting of strata (e.g., Jackson et al.,

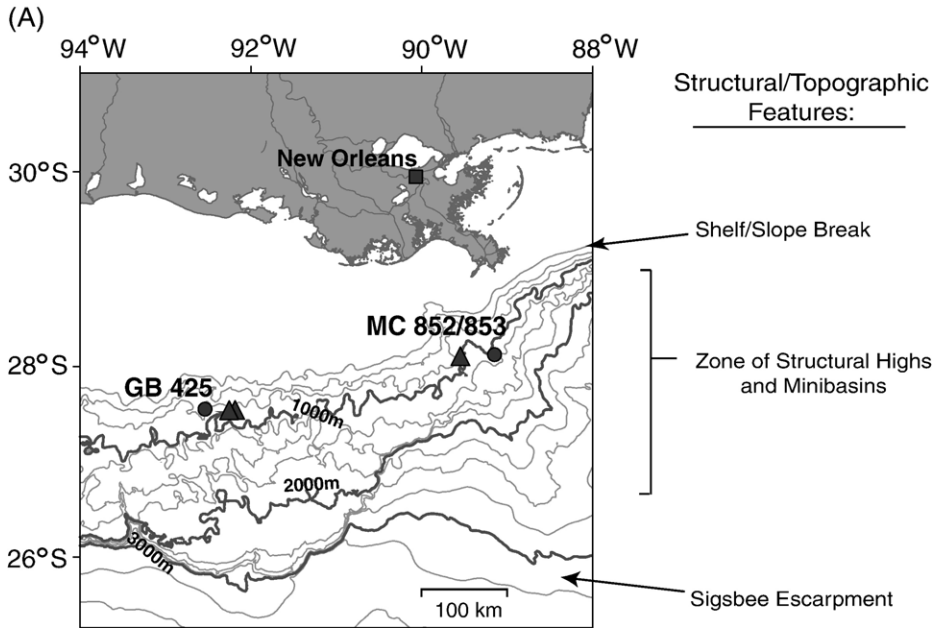

Fig. 3. Location maps for study areas in the Gulf of Mexico. (A) Regional map showing significant structural and topographic features. Sites included in this study are circles; other known barium-rich seeps are triangles (Fu and Aharon, 1998). (B) Bathymetric map of the mud volcano in Garden Banks lease block 425 (GB 425) and (C) the mud volcano on the boundary of Mississippi Canyon lease blocks 852 and 853 (MC 852/853). The locations of the cores are shown as two numbered circles. Bathymetry is in meters.

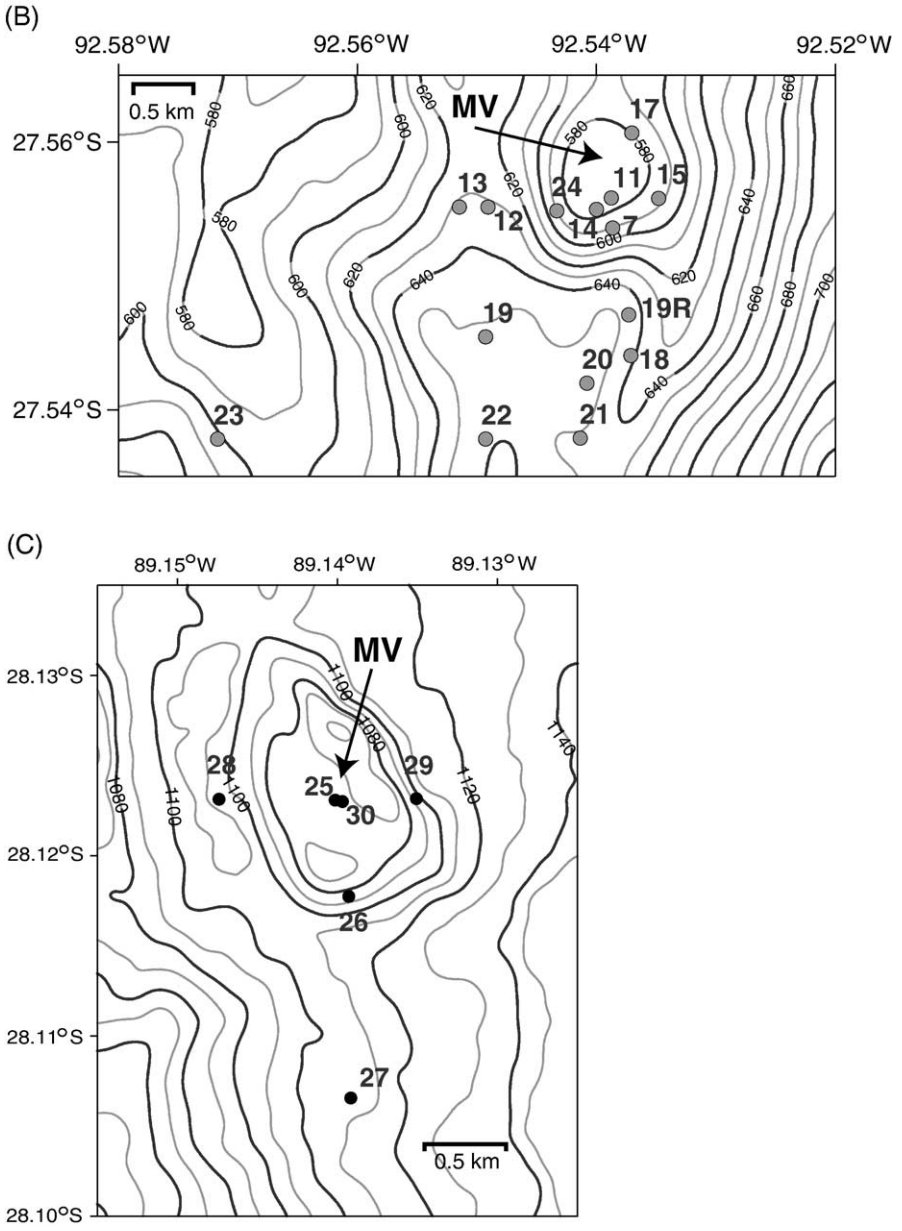

Fig. 3 (*continued*).

1994; Rowan et al., 1999), as well as the upward migration of fluids (Roberts and Nunn, 1995; Revil and Cathles, 2002). The phenomenon may be related because changes in fluid pressure can cause faults to expand and contract (Roberts and Nunn, 1995; Revil and Cathles, 2002). In the GOM, basinal fluids are often mixtures of hydrocarbon-rich brines and mud. The brines form as residual waters or when salt dissolves at depth; and they contain greatly elevated concentrations of Cl^-, Ca^{2+}, Na^+, K^+, Br^- and trace metals, including Pb, Zn, Mn and Ba (e.g., Manheim and Bischoff, 1969; Kharaka et al., 1987; Macpherson, 1989). As the fluids rise along expulsion pathways, they incorporate mud from unlithified strata (O'Brien, 1968). Potentially, fluidized muds can be derived from different depths than the hydrocarbons, and may represent material from a range in geologic time (Kohl and Roberts, 1994). Ultimately, seeps and mud volcanoes form where these fluids rise from depth and breach the seafloor (e.g., O'Brien, 1968; Neurauter and Bryant, 1990; Roberts and Aharon, 1994; Milkov and Sassen, 2002).

Fluids emanating from seeps and mud volcanoes in the GOM can have a distinct chemistry. Often, gases are dominated by CH_4 but contain high concentrations of other light hydrocarbons (C_2–C_6), consistent with a deep, thermogenic origin (Reitsema et al., 1978; Roberts et al., 1990; MacDonald et al., 2000; Milkov and Sassen, 2002; Sassen et al., 2003). The shallow fluids also have high concentrations of dissolved species found in brines (Fu and Aharon, 1998). Notably, elevated Ba^{2+} concentrations have been reported in pore waters from the upper 40 cm of sediment at a few sites of fluid seepage on the upper slope (Fu and Aharon, 1998).

4. Site description and sampling

4.1. Site description

Two bathymetric features characterized by active fluid expulsion were examined in this study: one is located in Garden Banks lease block 425 (GB 425) at 27.555°N, 92.540°W on the upper slope between 550 and 600 m water depth; the other is located on the border between Mississippi Canyon lease blocks 852 and 853 (MC 852/853) at 28.123°N, 89.140°W in a submarine canyon at water depths between 1010 and 1100 m (Fig. 3). The features are about 11 km (Garden Banks) and 59 km (Mississippi Canyon) away from the previously documented locations with seafloor barite and crusts (Fig. 3).

Both features have been variously referred to as mud mounds, seeps or mud volcanoes (e.g., Sager et al., 1999; Milkov and Sassen, 2002; Thomas, 2003; Ruppel et al., 2005). Although distinction between these terms is not always clear in the GOM (Neurauter and Bryant, 1990), we prefer the latter. Mud volcanoes are generally described as being significant bathymetric edifices, often circular to elliptical in shape, with a central conduit, and visible expression of fluid (including mud) expulsion (e.g., Neurauter and Roberts, 1994; Milkov, 2000; Dimitrov, 2002). Extensive studies show these characteristics for the features at GB 425 and MC 852/853 (Sager et al., 1999; Thomas, 2003; Ruppel et al., 2005). Both features are moderately large (>1 km) and roughly elliptical bathymetric highs, with relief above the surrounding seafloor exceeding 80 m at GB 425 and 40 m at MC 852/853 (Fig. 3). Chaotic reflectors and bright spots on 3-D seismic profiles suggest the presence of fluidized mud and hydrocarbons beneath the structures, and the movement of these fluids along faults toward the seafloor (Thomas, 2003).

Table 1
Geographical information for cores taken from GB 425 and MC 852/853

Core	Latitude (N)	Longitude (W)	Water depth (m)	Core length (m)	Distance from center (m)[a]
GB 425					
GB-GC-7	27° 33.214′	92° 32.318′	568	1.1	520
GB-PC-11	27° 33.349′	92° 32.327′	564	1.2	270
GB-PC-12	27° 33.310′	92° 32.945′	625	2.0	1071
GB-PC-13	27° 33.309′	92° 33.088′	627	2.9	1296
GB-PC-14	27° 33.299′	92° 32.399′	564	2.4	382
GB-PC-15	27° 33.347′	92° 32.087′	569	2.2	480
GB-PC-17	27° 33.640′	92° 32.221′	566	2.4	320
GB-PC-18	27° 32.643′	92° 32.227′	639	2.7	1586
GB-PC-19R	27° 32.743′	92° 32.227′	639	3.0	1402
GB-PC-19	27° 32.727′	92° 32.956′	647	3.5	1758
GB-PC-20	27° 32.579′	92° 32.447′	652	2.0	1708
GB-PC-21	27° 32.274′	92° 32.482′	642	3.7	2276
GB-PC-22	27° 32.269′	92° 32.956′	650	3.7	2494
GB-PC-23	27° 32.270′	92° 34.302′	587	1.8	3958
GB-PC-24	27° 33.291′	92° 32.598′	574	2.8	584
MC 852/853					
MC-PC-25	28° 7.380′	89° 8.381′	1067	1.7	47
MC-PC-26	28° 7.065′	89° 8.386′	1013	2.7	594
MC-PC-27	28° 6.393′	89° 8.350′	1098	4.0	1840
MC-PC-28	28° 7.388′	89° 8.827′	1093	1.6	683
MC-PC-29	28° 7.389′	89° 8.104′	1068	2.7	498
MC-PC-30	28° 7.385′	89° 8.409′	1070	3.5	0

[a] Distance from the center of the mud volcano was calculated using the latitude and longitude of estimated mud volcano center (from bathymetry maps) and the location of the cores.

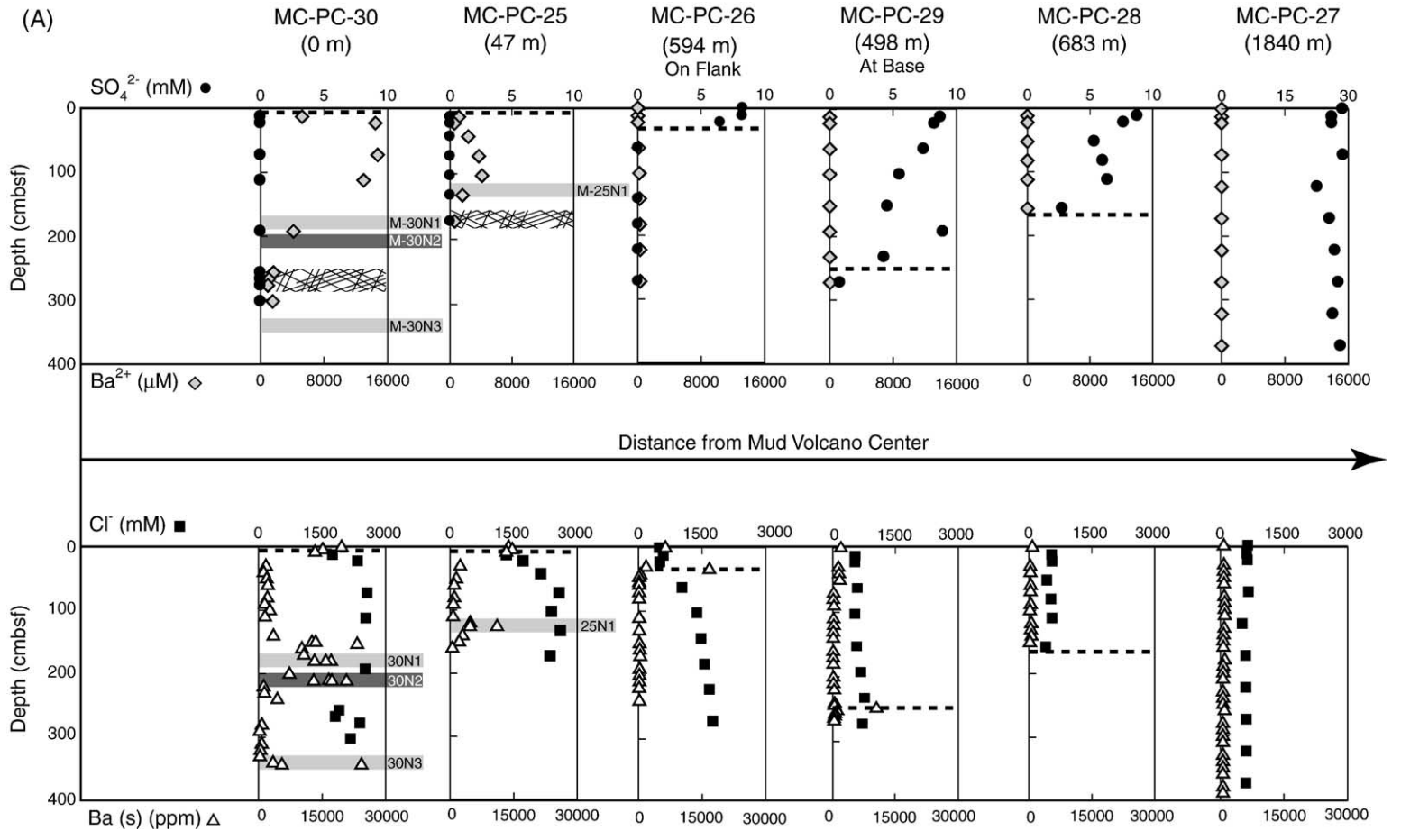

Fig. 4. Pore water profiles of dissolved barium, chloride and sulfate, and solid phase profiles of barium for cores in this study. (A) MC 852/853 and (B) through (D) GB 425. Profiles at each location have been plotted according to the distance from the center of mud volcanoes. Also shown on these plots are the inferred SHT horizons (dashed line), nodule horizons (light grey for rocky, dark grey for smooth) and zones where hydrate was detected (hatched areas). Please note that some cores only have data for dissolved species.

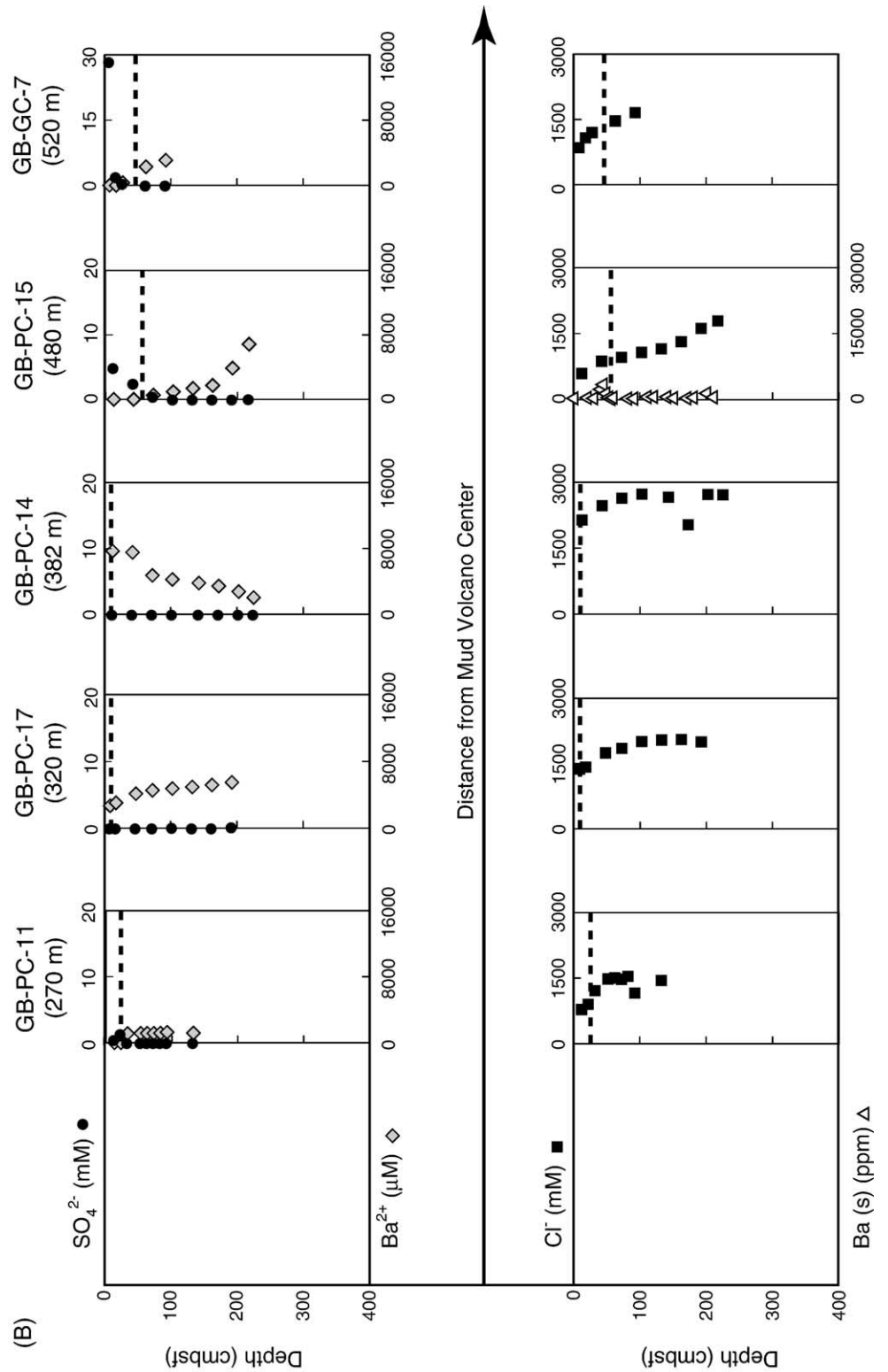

Fig. 4 (*continued*).

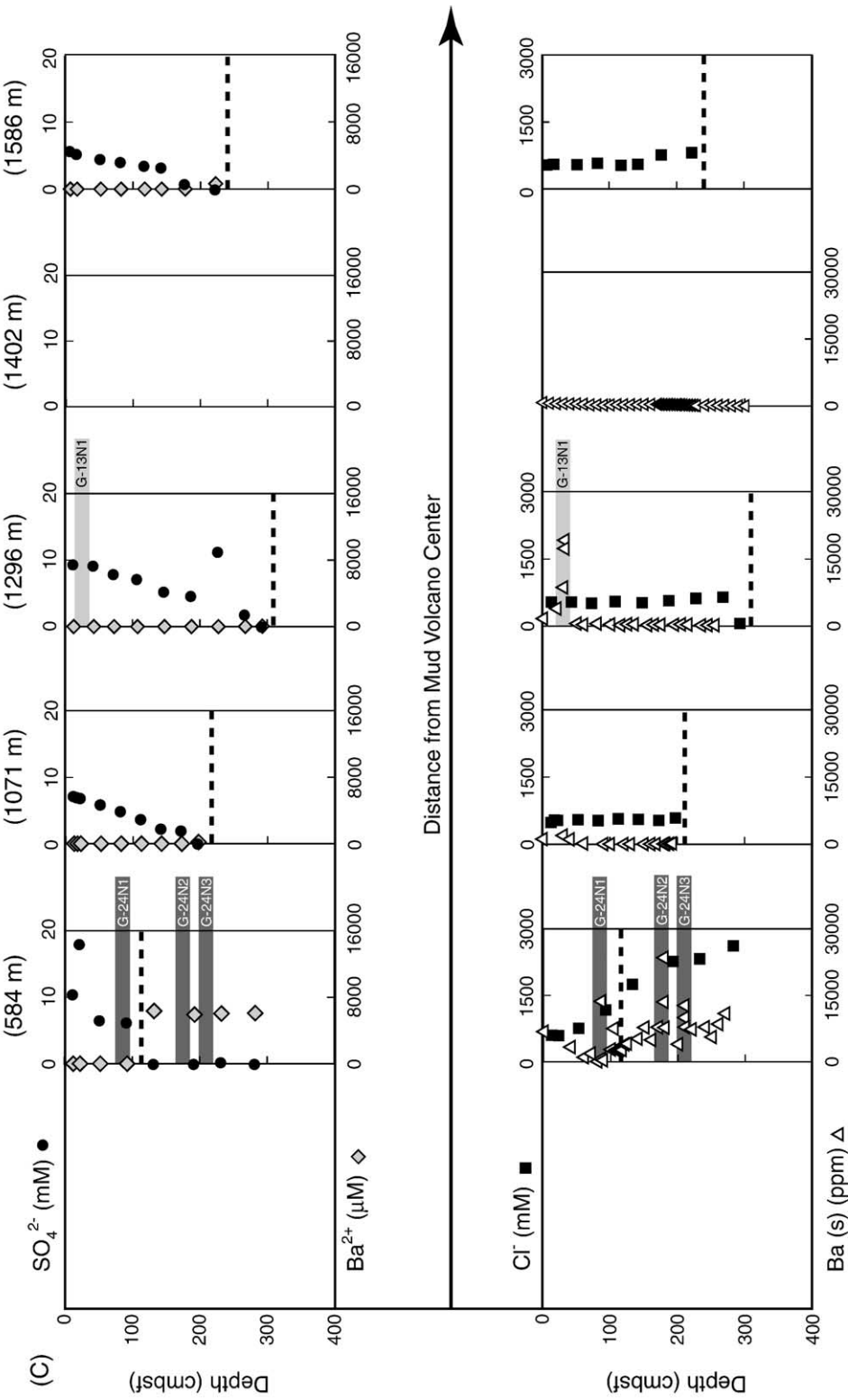

Fig. 4 (*continued*).

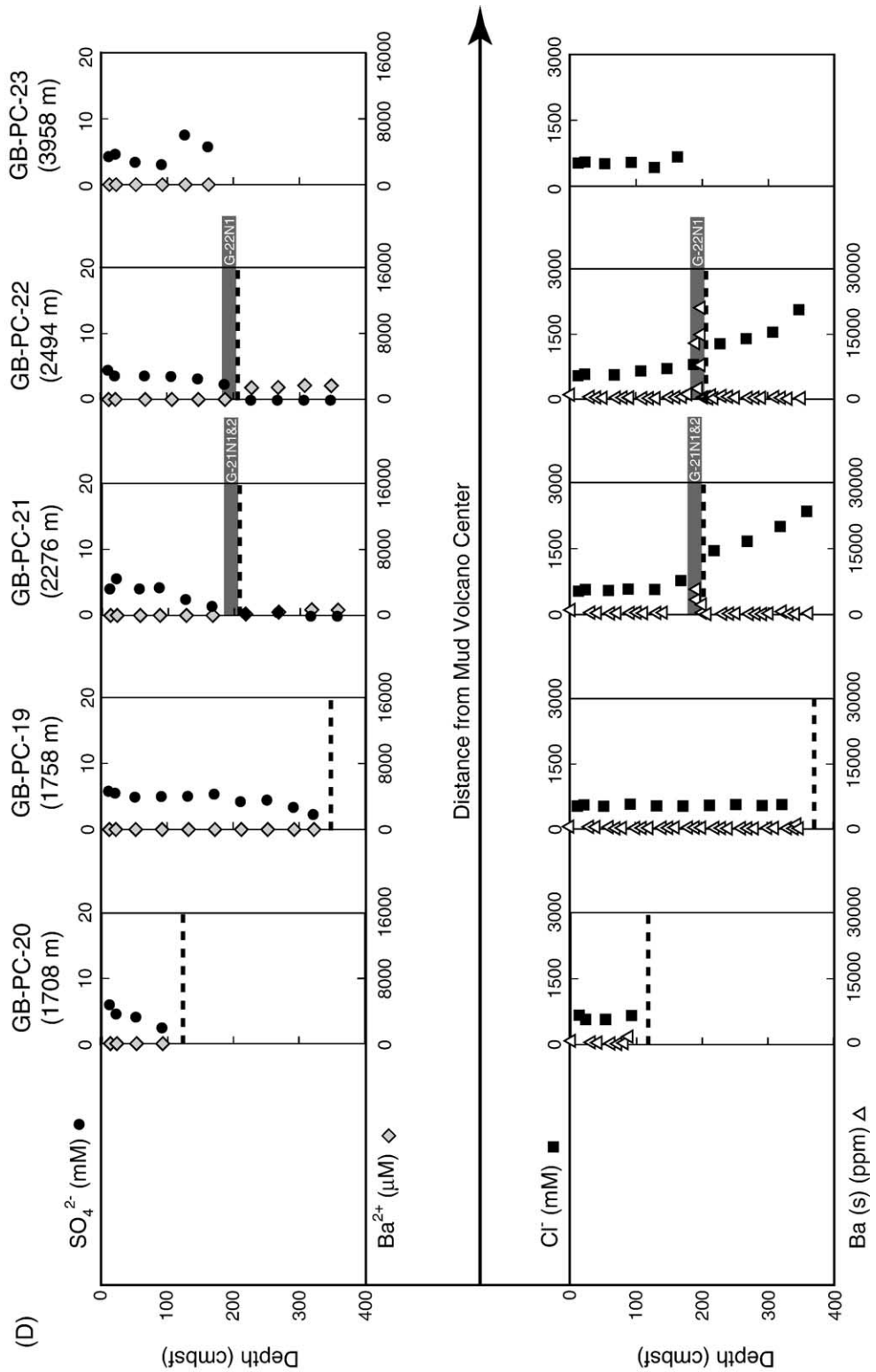

Fig. 4 (*continued*).

High rates of upward fluid advection are consistent with the extreme flux of heat across the structures (Ruppel et al., 2005). Seismic data also indicate recent deposition of mudflows around the features (Thomas, 2003).

Mud volcanoes at GB 425 and MC 852/853 (and in the GOM in general) are thought to form as the result of overpressured fluids migrating along faults above salt structures (e.g., Neurauter and Bryant, 1990; Neurauter and Roberts, 1994; Roberts and Aharon, 1994; Milkov and Sassen, 2002; Thomas, 2003). Although they probably formed under generally similar processes (e.g., Thomas, 2003), the two mud volcanoes examined in this study have different characteristics that may affect chemistry near the seafloor. First, the mud volcano at MC 852/853 (~1000 m) is in water twice as deep as the mud volcano at GB 425 (~550 m). Other factors (i.e., temperature, salinity, gas composition) being equal, the gas hydrate stability zone is thinner at GB 425 (Milkov and Sassen, 2002; Ruppel et al., 2005). Second, recent heat flow measurements suggest a higher flux of heat at GB 425 (Ruppel et al., 2005).

4.2. Sample collection

Cruise 08/02 of the *R/V Seward Johnson I* (October 17 through November 1, 2002) was dedicated to understanding physical and chemical fluxes around vent structures on the northern slope of the GOM. The main tool for obtaining sediment was a piston corer (PC) deployed as a gravity corer for mechanical reasons. At GB 425, 15 cores were collected in a "T" pattern across the mud volcano (Fig. 3b). A similar coring strategy was employed at MC 852/853, although only six cores were collected (Fig. 3c). The location, water depth, length and proximity to the center of the mud volcano have been compiled for each core (Table 1). Core lengths at both sites ranged from 1.1 m to 4.0 m (Table 1).

Upon retrieval, cores were immediately inspected for gas hydrates both visually and using a handheld infrared camera (ThermaCAM 2000 by FLIR systems; Ford et al., 2003). Intervals of gas hydrate were detected in two cores from MC 852/853, MC-PC-25 and MC-PC-30 (Weinberger, unpublished data) (Fig. 4). This observation is important because gas hydrate dissociation during core recovery releases fresh water, which can dilute dissolved constituents in pore water (Hesse and Harrison, 1981; Egeberg and Dickens, 1999). The presence of gas hydrate within 3 m of the seafloor also implies a steep hydrocarbon concentration gradient.

Whole-round sediment intervals were cut from cores on deck for pore water sampling. To minimize oxidation, these were transported immediately to a shipboard chemistry laboratory for pore water extraction. Samples were trimmed to remove sediment contamination and placed into a modified Reeburgh squeezing vessel (Reeburgh, 1967) pressurized with N_2 at 40 psi. The Reeburgh system uses gas pressure against rubber diaphragms to squeeze interstitial fluids from sediment through a series of filtering membranes and into a syringe. Once collected, pore waters were filtered again with a Low Protein Binding Durapore (PVDF) membrane (0.22 μm). The first 1 mL aliquot was taken for shipboard salinity measurements. A second 2 mL aliquot was treated with 0.01

Table 2
Location and mineralogic composition of nodules

Nodule	Core	Depth (cmbsf)	Major peak	Major peak intensity (CPS)	Secondary peak	Secondary peak intensity (CPS)	Minor peaks
Rocky							
G-13N1	GB-PC-13	32–34	Barite	900	Aragonite	518	(Pb-rich) barite
M-25N1	MC-PC-25	125–128	Calcite	3299	High-Mg calcite	576	
M-30N1	MC-PC-30	180–182	Calcite	2633	Barite	293	Quartz
M-30N3	MC-PC-30	343–345	Calcite	2691	Barite	581	High-Mg calcite
Smooth							
G-21N1	GB-PC-21	190–192	Calcite	3381	High-Mg calcite	726	
G-21N2	GB-PC-21	200	Calcite	3381	High-Mg calcite	726	
G-22N1	GB-PC-22	198–200	Calcite	1841	Barite	557	High-Mg calcite
G-24N1	GB-PC-24	85–88	Calcite	3434	High-Mg calcite	464	
G-24N2	GB-PC-24	179–180	Calcite	2943	Barite	452	(Pb-rich barite), Quartz, Aragonite
G-24N3	GB-PC-24	209–212	Calcite	3139	Hi-Mg calcite	570	
M-30N2	MC-PC-30	208–210	Calcite	1347	(Pb-rich) barite	869	High-Mg calcite, quartz

Notes: Intensity is measured in counts per second (CPS). Minor mineral phases are listed in order of abundance. Pb-rich barite was detected but not confirmed with chemical data.

mL of concentrated, ultrapure HNO_3 to inhibit metal precipitation, and stored in a sealed glass vial for shorebased Ba analyses. A third 2 mL aliquot was purged with N_2 gas for 1 min to degas dissolved sulfide, and sealed in a glass vial for shorebased anion measurements. We note that infusion of oxygen during sample collection and storage in glass vials do not affect pore water Ba concentrations, at least at the levels anticipated (and measured) in this study.

Unsampled core intervals were temporarily stored in a refrigerated van on the ship and subsequently transferred to a cold room (~4.5 °C) at Georgia Tech for shore-based description and sampling. Cores were described visually for their sediment color, grain size and texture. The most striking observation in general core descriptions is the presence of cm-scale nodules, which were found in six of the cores (Table 2).

Bulk sediment samples of ~3 cm^3 were taken down 15 of the cores for chemical analyses. Typically, these samples were spaced every 10 cm. However, using the pore water Ba^{2+} and SO_4^{2-} profiles (discussed in the following sections), the SHT was inferred in 10 of these cores (and 18 of 21 cores in total). Samples were taken every 2 cm through these zones. All nodules were also removed for chemical and mineralogical analyses.

5. Laboratory analyses

5.1. Pore fluid analysis

Salinity was measured on the ship using a handheld refractometer scaled at 0–100‰. For those pore water samples with $S>100$‰, samples were diluted 1:1 with deionized water. The aliquots taken for anion analyses were also re-examined on shore with a refractometer to verify shipboard measurements, and to determine whether evaporation had occurred. Salinity measurements were reproducible within 5% (Appendix A), indicating that minimal water loss occurred during transport and storage.

Pore water Cl^- and SO_4^{2-} were analyzed using a Dionex Ion Chromatograph (IC) system with an IonPac AS11-HC column using 26.5 nM NaOH eluent at the Environmental Engineering Laboratory, Rice University. Concentrations were determined by comparing sample peak intensities to standard peaks having known concentrations. All Cl^- concentrations were reproducible within 10% of one another (Appendix A), even at high concentrations ($Cl^->2700$ mM).

The precision of SO_4^{2-} concentrations was highly variable. The basic problem was determining low SO_4^{2-} concentrations in waters of extremely high salinity ($S>100$‰), which compromises SO_4^{2-} detection on the IC. It was hoped that different operating conditions on a different instrument could improve SO_4^{2-} measurements. Consequently, all fluid samples were re-measured on a Dionex IC in the Laboratory for Oceanographic and Environmental Research (LOER), Texas A&M University, Galveston. These SO_4^{2-} measurements also had low precision at low concentrations. As a result, SO_4^{2-} profiles presented in this paper are only valid in the general sense.

Pore water Ba^{2+} concentrations were analyzed using a Varian Vista Pro ICP-AES in the Geochemistry Laboratory at Rice University with a wavelength of 455.403 nm. Concentrations were determined by comparing peak areas to those determined by analyzing standard solutions with a similar NaCl matrix and known Ba^{2+} concentrations. A calibration run measuring standards and blanks was made prior to every 15 samples. An internal standard of Yttrium (1 ppm) was also added to all standards and samples to monitor any instrumental drift. The precision of reported Ba^{2+} concentrations was determined by analyzing true replicates. Multiple analyses of samples consistently gave concentrations within 4% for each element.

5.2. Sediment analysis

Sediment samples were washed three times with deionized water (18 MΩ) to remove dissolved ions, freeze-dried to remove water, and ground with a mortar and pestle. Approximately 0.1 g subsamples were weighed and digested in a solution containing 9.0 mL concentrated HCl and 3.0 mL concentrated HNO_3 for approximately 18 h in a 70 °C water bath. The digested solution was decanted and diluted with deionized water. This solution is assumed to comprise the "extractable", non-terrigenous fraction of sediment; this fraction may include elements released from barite, as well as oxyhydroxides, sulfides, and carbonates. The remaining terrigenous (aluminosilicate) fraction (Rutten and de Lange, 2002) was not analyzed in this study. Digested solutions were then analyzed for Ba^{2+} on the ICP-AES according to the procedure above. The precision of these measurements was determined by digesting and analyzing true replicate samples, and is within 5% for each element.

After measuring the extractable Ba content, five sediment samples from cores at MC 852/853 and containing variable amounts of Ba were subjected to a sequential extraction (Paytan et al., 1993; Eagle et al., 2003). The purpose of these extractions was to assess

whether barite is the dominant carrier of Ba in certain sediment samples. Briefly, the extraction involved a series of 24-h treatments using acetic acid, sodium hypochlorite solution, hydroxylamine hydrochloride solution, nitric acid and hydrofluoric acid. A barite standard was also subjected to this extraction procedure to determine how the process affected barite crystals. After extractions, residual material was weighed and examined using a JEOL JXA 840 Scanning Electron Microscope (SEM) equipped with a Energy Dispersive Spectometer (EDS) at Rice University.

5.3. Nodules

Nodules were rinsed with deionized water to remove surrounding mud, photographed, and split in half with a trim saw. One half of each nodule was dried overnight in an oven at 80 °C and then ground, powdered, digested and analyzed for elemental chemistry by ICP-AES as described above. Bulk mineralogy was also determined on a portion of the washed powder using a D/Max 2000/PC Rigaku X-ray Diffraction (XRD) system equipped with a fixed monochromator in the Geochemistry Laboratory at Rice University. Samples were measured using a continuous scan from 20 to 50 2θ at 40 kV and 40 mA. The other halves of the concretions were used to make thin sections to assess their general fabric and texture. Thin sections were examined using a petrographic microscope and the aforementioned SEM–EDS system.

6. Results

6.1. Pore fluid chemistry

Pore water salinity (S) ranges from 35‰ to 130‰ at both GB 425 and MC 852/853 (Appendix A). Chloride covaries with S at both sites ($r^2 > 0.90$), ranging from 500 to 2700 mM (Appendix A; Fig. 4). The extreme highs in S and Cl^- come from the base of cores taken within 300 m of the mud volcano centers; the lower values, approaching those of seawater, come from near-surface sediment and from outlying cores. Depth profiles of S and Cl^- that terminate at extremely high concentrations (e.g., cores MC-PC-25 and MC-PC-30) are concave-down, suggesting strong upward fluid advection. This is consistent with heat flow measurements across the mud volcanoes (Ruppel et al., 2005). By contrast, S and Cl^- depth profiles characterized by generally low concentrations (e.g., in GB-PC-15, GB-PC-21, and GB-PC-22) are either concave-up, suggesting downward hydrologic flow (Ruppel et al., 2005), or straight, indicating a more diffusive regime (Fig. 4). Overall, the shapes of S and Cl^- profiles vary with respect to mud volcano proximity similarly at GB 425 and MC 852/853.

Sulfate concentrations range from 28 mM to below detection (<0.10 mM) at both GB 425 and MC 852/853 (Appendix A). Unlike S and Cl^-, however, SO_4^{2-} concentrations are generally lowest near the center of the mud volcanoes. Cores closest to venting sites have SO_4^{2-}concentrations <5 mM within 10 cm below the seafloor (cmbsf), suggesting that SO_4^{2-} consumption occurs at or very close to the sediment–water interface, as observed at other GOM seep sites (Aharon and Fu, 2003; Joye et al., 2004). In cores taken from flanks of the mud volcanoes, however, a decreasing SO_4^{2-} gradient can be observed from seawater concentrations (~28 mM) at the sediment–water interface. In some cores, this gradient is sufficiently high so that SO_4^{2-} drops below 0.10 mM within the core. This depth, presumably the SHT, depends on proximity to the mud volcano. In general, the inferred SHT deepens away from the mud volcanoes (Fig. 4). Overall, an inverse relationship exists between SO_4^{2-} and Cl^-. Concentrations of SO_4^{2-} are measurable where Cl^- values are near those of seawater; SO_4^{2-} is <0.10 mM where Cl^- concentrations exceed twice that of seawater (1120 mM).

Dissolved Ba^{2+} concentrations are extremely high in pore waters at the mud volcanoes, reaching 7800 μM at 171 cmbsf in Core GB-PC-24 and 12,000 μM at 72.5 cmbsf in Core MC-PC-30 (Appendix A). By contrast, Ba^{2+} concentrations are <2.0 μM in pore waters collected from the upper 200 cm of cores away from the mud volcanoes. However, in some cores from the flanks of the mud volcanoes, Ba^{2+} concentrations do increase significantly with depth, reaching 1700 μM at 347.5 cmbsf in Core GB-PC-22, and 330 μM at 272 cmbsf in Core MC-PC-26. Generally, dissolved Ba^{2+} concentrations are uniformly low (<3 μM) above the inferred SHT, but increase rapidly below this horizon (Fig. 4). A notable exception occurs in the two cores from the center of the mud volcano at MC 852/853. In MC-PC-25 and MC-PC-30, pore water Ba^{2+} concentrations are very high in shallow sediment, but decrease down-core.

6.2. Sediment chemistry

The extractable Ba content of most sediment examined, especially from cores away from the mud volcanoes, ranges from 70 to 2000 mg/kg (Appendix B). Superimposed on these modest “background” Ba

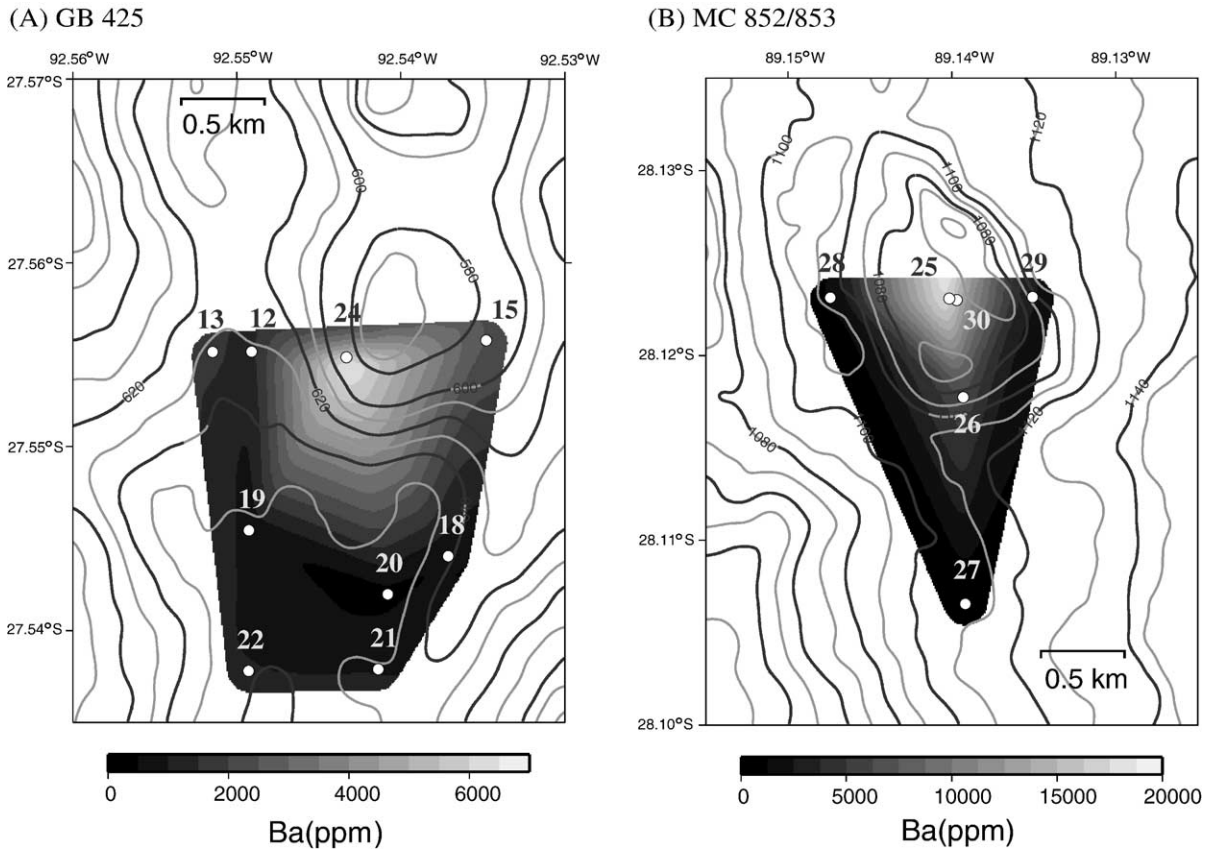

Fig. 5. Barium content of the upper 2 cm of sediment around the mud volcanoes. (A) GB 425 and (B) MC 852/853. At both sites, solid barium content is greatest at the center of the mud volcano and decreases away from the venting.

contents, however, are discrete horizons of significantly elevated Ba in eight of the cores (Fig. 4). Three cores (GB-PC-24, MC-PC-25 and MC-PC-30) have two to four maxima where solid phase Ba content reaches between 14,600 and 23,000 mg/kg. Another five cores (GB-PC-15, GB-PC-21, GB-PC-22, MC-PC-26 and MC-PC-29) have a single peak where Ba content exceeds 20,000 mg/kg. The depths of these sedimentary Ba peaks closely correspond with (1) the depth of SO_4^{2-} depletion (and the inferred SHT), (2)

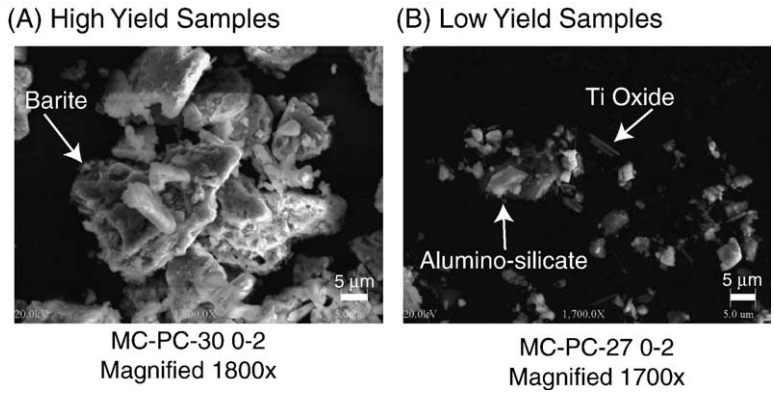

Fig. 6. Residual sediment after sequential extraction for barite. (A) Showing abundant barite in high yield samples (>13%) and some other minerals, including titanium oxides and alumino-silicates. Note the pitted and rounded nature of the barite crystals, which may result from the extraction procedure. (B) Low yield samples (<3%) with negligible barite, but common alumino-silicates and titanium oxides.

horizons containing nodules, or (3) both (Fig. 4). Like pore waters, the solid phase "background" Ba content as well as the number and magnitude of Ba maxima are greatest at the center of the mud volcanoes and diminish outward. As a result, a concentric pattern of Ba content exists in sediment around the mud volca-

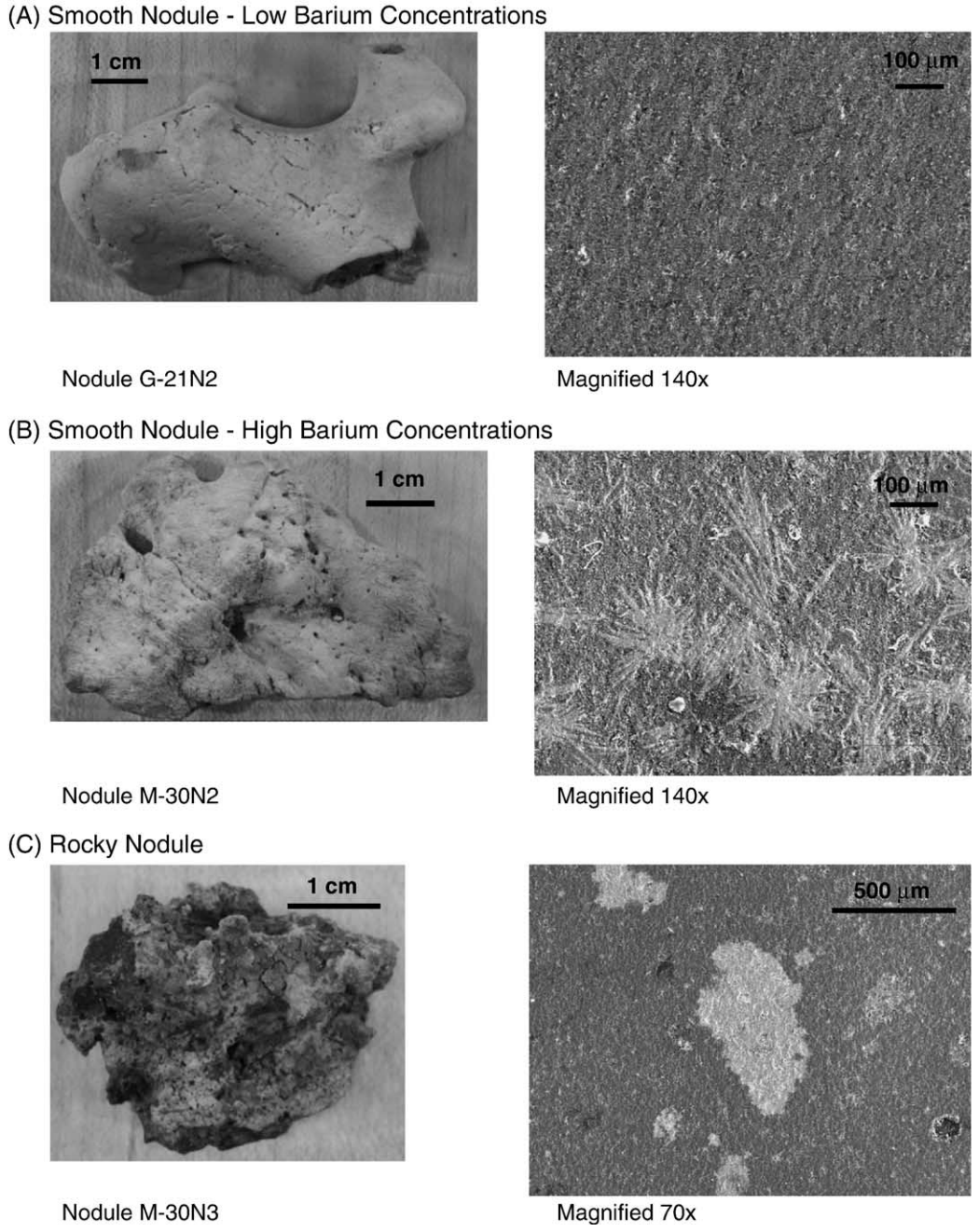

Fig. 7. Images of whole nodules and representative thin sections. (A) Smooth nodule from core GB-PC-21, (B) smooth nodule from core MC-PC-30, and (C) rocky nodule from MC-PC-30. In hand sample, all smooth nodules look similar in texture and have an oblong morphology. However, SEM-EDS images (magnified 140× when taken) reveal a distinct difference in crystal structure. Nodules from areas with higher venting rates (B) yield higher barium content and distinct barite crystals (light gray) that are acicular and organized in radial patterns. Barite crystals are small and blocky (A) in nodules from areas with lower venting rates and lower barium content. The rocky nodule (C) has a distinctly different morphology to smooth nodules. SEM images (magnified 70× when taken) show in-filling textures where barite is a secondary mineral phase within large void spaces.

noes, even in samples within 2 cm of the seafloor (Fig. 5).

Sequential extractions show that barite dominates the Ba-rich sediment intervals. After the procedure to isolate barite, samples from Ba maxima (MC-PC-30, 0–2 cm and 170–172 cm) had the greatest proportion of material mass remaining (>13%). Moreover, barite crystals, up to 15 μm in width, are very common in these high yield extractions (Fig. 6). By contrast, samples of sediment with low total Ba contents (MC-PC-27, 0–2 cm; MC-PC-30, 50–52 and 140–142 cm) render relatively low masses of material after extraction (<3%). These residues also have little to no barite. Instead, SEM examinations show that these residues are primarily titanium oxides and alumino-silicate minerals, such as clays (Fig. 6).

6.3. Nodules

Nodules found in the cores can be described as either rocky or smooth, depending on morphology and texture (Fig. 7). Rocky nodules are rough conglomerates with sand, fossil fragments and other debris welded together in a grey matrix with large macroscopic voids. These nodules are friable and crumble easily. Smooth nodules have a homogeneous surface, generally elongated shape, and consist of well-sorted sand in a mud matrix. Smooth nodules are also more consolidated than rocky nodules. In the 15 cores examined, four rocky nodules and seven smooth nodules were recovered from a total of six cores (Table 2).

Both rocky and smooth nodules comprise variable amounts of six minerals, at least as detected by XRD (Table 2). Calcite dominates all of the nodules with the exception of nodule G-13N1, which is predominately composed of barite. Assuming that peak areas on diffraction profiles are related to mineral abundances, barite is the second most abundant mineral in five nodules. In the other five nodules, barite was not detected by XRD. Other accessory minerals in the nodules include high-magnesium calcite, aragonite and quartz. It is interesting to note, though, that quartz was only found in nodules from cores close to the mud

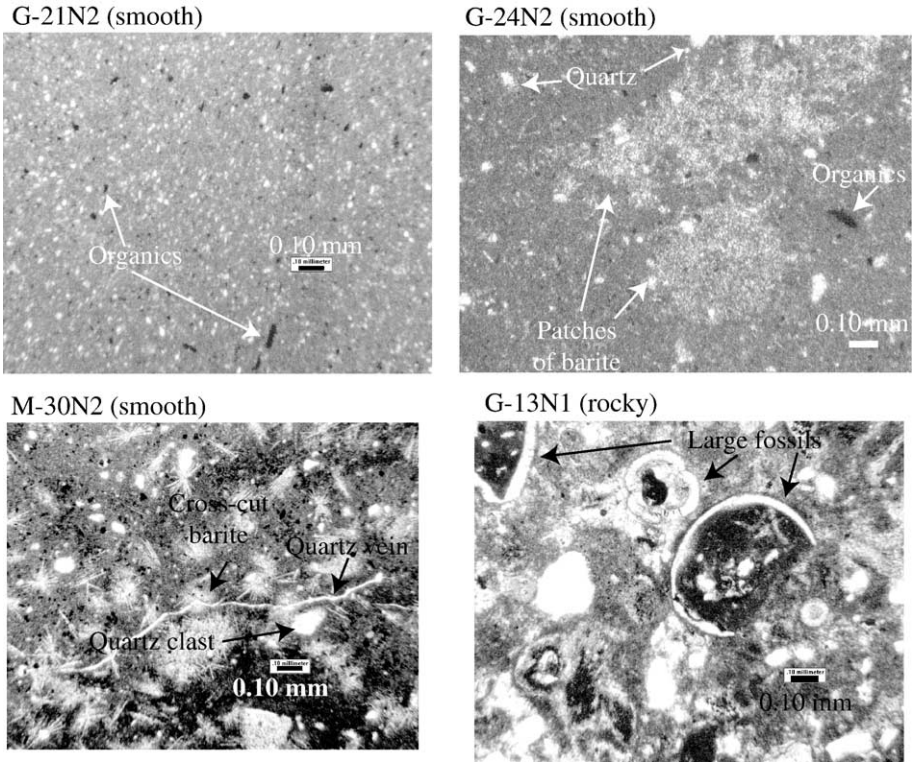

Fig. 8. Photomicrographs of smooth and rocky nodules. Smooth nodules from low flux environments (G-21N2) are fine grained with organics and quartz. Smooth nodules from high flux environment show well-developed barite crystals (G-24N2, M-30N2) that are often cross-cut by quartz veins (M-30N2). Quartz veins exhibit undulating extinction, suggesting some thermal alteration. Some rocky nodules (G-13N1) show a wealth of microfossils with carbonate clasts and quartz grains supported by a carbonate matrix.

volcanoes. Some of the barite reported for six of the nodules are lead-rich according to the d-spacing determined through XRD; however, this was not confirmed with chemical data.

Rocky nodules in thin section (Figs. 7 and 8) are amalgamations of well-rounded carbonate clasts and abundant quartz grains of variable size (20–200 μm) and roundness. Microfossils are common, and include foraminifera and bi-valve fragments. Brown organic material (presumably kerogen; Fu and Aharon, 1997) also exists near the outer edges of nodules. Importantly, copious void spaces in these nodules are filled with small, blocky barite crystals. This barite in-filling is most complete in the deepest rocky nodules.

In contrast, smooth nodules in thin section have a relatively uniform carbonate matrix containing barite crystals, quartz grains and quartz veins (Figs. 7 and 8). Barite occurs in two crystal habits, which appear to correspond to the concentration of dissolved Ba^{2+} in surrounding pore waters. In Ba-rich waters at the center of mud volcanoes, acicular barite crystals (150–200 μm) form radial patterns. Conversely, in Ba-poor waters on the volcano flanks, small blocky barite crystals (<10 μM) are scattered throughout the matrix. Quartz grains vary in size, but are typically <10 μm and finer than those in rocky nodules. Many of these grains are secondary, showing undulating extinction and forming veins that cross-cut acicular barite crystals (Fig. 8).

Given the above mineralogy and thin section descriptions, it is not surprising that nodules contain high contents of Ba, ranging from 460 to 24,000 mg/kg (Appendix B). It is noteworthy that nodules with the smallest barite peaks on XRD traces also have the lowest Ba contents. Interestingly, the Ba content of rocky nodules in core MC-PC-30 increases with depth. The shallow rocky nodule has 17,000 mg/kg Ba, whereas the deep rocky nodule has 24,000 mg/kg Ba.

7. Discussion

7.1. Sulfate–hydrocarbon transition across mud volcanoes

The relationship between pore water CH_4 and SO_4^{2-} concentrations is well documented for gas-charged sediment along continental margins, at least at regional scale (Borowski et al., 1999; D'Hondt et al., 2002). In general, SO_4^{2-} drops from ~28 mM at the seafloor to ~0 mM at some relatively shallow depth. Below this depth – the SHT – dissolved CH_4 increases rapidly. In systems dominated by diffusion, such as Blake Ridge, the SHT typically occurs between 5 and 50 mbsf (Borowski et al., 1996, 1999; D'Hondt et al., 2002). Multiple lines of evidence suggest that the depth of the SHT depends on the upward CH_4 flux at these locations (Borowski et al., 1996, 1999; Dickens, 2001). The SHT is much shallower in systems dominated by fluid advection, sometimes occurring within the upper 30 cmbsf (Tsunogai et al., 2002; Aharon and Fu, 2003; Haese et al., 2003). Consumption of SO_4^{2-} in these environments also involves significant amounts of higher hydrocarbons (Formolo et al., 2004; Joye et al., 2004), so that the SHT probably reflects total hydrocarbon flux instead of just CH_4. Nevertheless, the SHT should shoal significantly across a mud volcano (Fig. 1).

Methane and other hydrocarbon concentrations were not measured in this study. Given the ubiquitous relationship between hydrocarbon gas and SO_4^{2-} profiles found elsewhere, however, the SO_4^{2-} profiles can be used to infer the SHT (Fig. 4). Specifically, the SHT is placed at the depth where pore water SO_4^{2-} drops to below detection. With this assumption, the inferred SHT lies at or near the sediment–water interface at the center of mud volcanoes, and deepens on the flanks. Intense hydrocarbon expulsion at the center effectively pushes the SHT to the seafloor. With lower hydrocarbon fluxes on the flanks, SO_4^{2-} diffuses from overlying seawater into the sediment. Thus, a concentric variation in the depth of the SHT occurs at the local (<1 km) scale around mud volcanoes in the GOM (Fig. 1).

Several recent studies have tried to quantify the rates of AOM and SO_4^{2-} removal in sediment at seeps and mud volcanoes in the GOM (Aharon and Fu, 2000, 2003; Formolo et al., 2004; Joye et al., 2004). These investigations, generally using short cores over a limited area, have proposed that SO_4^{2-} reduction is coupled to CH_4 and hydrocarbon fluxing. This interpretation is consistent with the clear correlation between the location of venting and the inferred SHT depth (Fig. 4).

7.2. Barite fronts at the sulfate–methane transition

Characteristic dissolved Ba^{2+} and solid phase Ba profiles develop in diffusive systems where barite dissolves and re-precipitates across a horizon of very low pore water SO_4^{2-} concentrations (Fig. 2). Although initially discussed without consideration of CH_4 cycling (Brumsack, 1986; Torres et al., 1996a), these Ba profiles are clearly coupled to the SHT (Dickens, 2001; Aloisi et al., 2004; Kasten et al., 2004; Snyder et al., in press). Above the SHT, dissolved Ba^{2+} concentrations are very low and some barite occurs in sediment through pelagic accumulation. Below the SHT, dis-

solved Ba^{2+} rapidly increases as the barite dissolves. A front of labile Ba forms just above the SHT when dissolved Ba^{2+} released at depth migrates up and precipitates as barite upon contact with seawater SO_4^{2-}.

The expected Ba profiles are observed in sediment around mud volcanoes in the GOM. Of the 15 cores examined, eight contain a discrete horizon of elevated sedimentary barium that lies within 0 to 30 cm above the inferred SHT (Fig. 4). Pore water Ba^{2+} concentrations in these cores are less than 3.0 μM above barium fronts, but increase by three to four orders of magnitude immediately below. Sulfate does not drop below 2.5 mM within the other seven cores, and neither a solid Ba front nor a rise in dissolved Ba^{2+} is observed (although both likely occur deeper beyond the length of the cores).

In theory, the solid phase Ba front immediately above the SHT should comprise barite (Fig. 2), although this has rarely been demonstrated (Snyder et al., in press). All data in this paper indicate that Ba cycles across the inferred SHT because of barite dissolution and precipitation. Certainly, the sequential extractions of sediment from cores in this study, albeit limited, confirm that barite dominates the solid Ba fronts (Fig. 6). Moreover, because the upward flux of hydrocarbons controls the interstitial SO_4^{2-} concentration profiles, hydrocarbons also dictate dissolved Ba^{2+} concentrations and the presence of barite.

Barium cycling in sediments around mud volcanoes in the GOM is generally analogous to that found or predicted at other deep-sea locations (Brumsack, 1986; Torres et al., 1996a; Dickens, 2001; Aloisi et al., 2004; Kasten et al., 2004; Snyder et al., in press). However, this cycling is more complicated than implied in current literature (e.g., Dickens, 2001). First, basinal fluids driving mud volcanism contain significant concentrations of Ba^{2+}. Thus, not all Ba comes from the surface. Second, barite-rich carbonate nodules are found below the inferred SHT. These could provide a local source for Ba^{2+} when they dissolve. Third, expulsion of Ba^{2+} rich fluids into bottom water might occur during mud volcano eruptions. Potentially, this process amplifies overall Ba cycling. These complexities are discussed below.

7.3. Effect of deep brines and formation waters

Compared to seawater, formation waters collected from deep boreholes in the northern GOM are greatly enriched in Cl^- and a suite of major cations (e.g., Kharaka et al., 1987; Macpherson, 1989). These basinal brines also contain high dissolved Ba^{2+}, with concentrations between 45 and 30,000 μM (Macpherson, 1989). The elevated Cl^- concentrations probably result from dissolution of salt (Lands and Macpherson, 1992). The high Ba^{2+} concentrations may come from diagenesis of potassium-rich feldspars in arkosic sandstone horizons (Macpherson, 1989).

Pore waters from the center of the mud volcanoes have much higher dissolved Ba^{2+} concentrations than those reported from most marine environments, including other regions with gas-charged sediment. For example, at Blake Ridge, dissolved Ba^{2+} concentrations do not exceed 60 μM, even below the SHT (Snyder et al., in press). Here, it is important to highlight three observations (Fig. 9). First, both mud volcano pore waters and deep formation waters have high Cl^- and Ba^{2+} concentrations. Second, dissolved Cl^- and Ba^{2+} concentrations generally covary in both fluids. Third, pore water Cl^- concentrations at the mud volcanoes increase with depth from seawater values near the seafloor. Collectively, these observations suggest that upward fluid migration supplies large amounts of Cl^- and Ba^{2+}. At nearby mud volcanoes (Fig. 3), some pore fluid samples from the upper 40 cm of a few cores have been examined for Ba^{2+} and Cl^- concentrations as well as O, Sr, and S isotopic compositions (Fu and Aharon, 1998; Aharon et al., 2001). Correlations between the elemental and isotopic properties also suggest that significant amounts of Ba^{2+} come from depth (Fu and Aharon, 1998; Aharon et al., 2001).

Remobilized pelagic barite is often suggested as the main source for elevated dissolved Ba^{2+} and shallow barite fronts across the SHT (Brumsack, 1986; Torres et al., 1996a; Naehr et al., 2000; Dickens, 2001; Aloisi et al., 2004; Snyder et al., in press). Although pelagic barite may contribute Ba^{2+} to sediment around GOM mud volcanoes, fluids from below likely supply much of the Ba^{2+} to the system.

The Ba^{2+} contribution from deep formation waters to shallow sediment around mud volcanoes over time might be assessed using the accumulation and chemical composition of sediment, and the flux and dissolved concentrations of vent fluids. Significant curvature in the salinity (and heat) profiles above the mud volcanoes suggests strong upward advection of water, on the order of 0.05 to 0.15 m/year across MC 853/854 (Ruppel et al., 2005). Given the bathymetric expression of this mud volcano (~1 km^2), and the dissolved Ba^{2+} concentrations at the base of cores (300 to 1200 μM), formation waters may contribute around 0.03 to 0.12 mol/m^2-year of Ba^{2+} to shallow sediment at MC 853/854. This is orders of magnitude faster than Ba^{2+} is supplied to sediment from the pelagic rain of organic carbon (e.g., Pfeifer et al., 2001). The average extract-

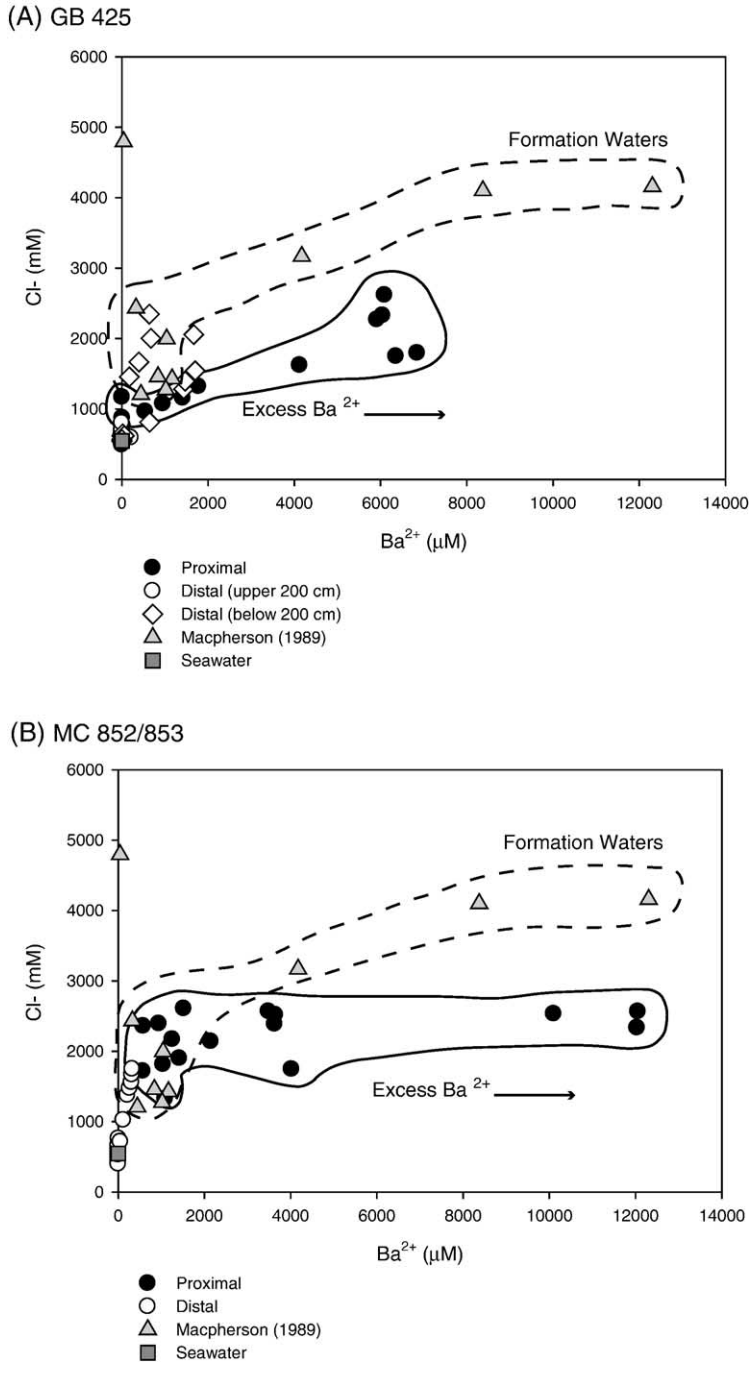

Fig. 9. Plot of dissolved barium and chloride for pore water from (A) GB 425, and (B) MC 852/853, formation waters (Macpherson, 1989) and seawater (Quinby-Hunt and Turekian, 1983). These plots show zones of distinct mixing between formation water and seawater, producing composite pore water values. However, in some cases, proximal pore waters are enriched with Ba^{2+} as a result of amplified barium cycling.

able Ba content in the upper few meters of sediment at MC 853/854 is difficult to assess because of the extreme heterogeneity (Fig. 5), although 1000 mg/kg seems reasonable (Appendix B). Formation fluids could supply this excess barium in about 1000 years.

Despite the high input of Ba^{2+} from below, the dissolved Cl^- and Ba^{2+} concentrations of relevant fluids reveal an additional constraint regarding Ba cycling in the time domain: for a given Cl^- concentration, formation waters generally contain less Ba^{2+}

than shallow pore waters at mud volcanoes (Fig. 9). The simplest explanation is that shallow pore waters hold excess dissolved Ba^{2+} compared to formation waters. Although upward advection of fluids supply much of the Ba^{2+} to shallow sediment at the GOM mud volcanoes, processes within the upper few meters of sediment cycle and retain this Ba^{2+} over time. This interpretation contrasts somewhat with previous work (Fu and Aharon, 1998), which assumed that high Ba^{2+} concentrations reflect similarly elevated concentrations at depth.

Depth profiles of dissolved Ba^{2+} from the center of the mud volcano at MC 852/853 hint at this shallow cycling and retention of Ba^{2+}. Both cores MC-PC-30 and MC-PC-25 have a marked rise in dissolved Ba^{2+} below an SHT inferred to occur at or near seafloor. However, dissolved Ba^{2+} concentrations then decrease toward those of formation waters toward the base of these cores (Figs. 4 and 9). Evidently, dissolved Ba^{2+} is being released and consumed in the upper few meters of sediment at the mud volcanoes.

7.4. Carbonate nodules

The barite-rich nodules found at the center of the mud volcanoes (Figs. 7 and 8) complicate ideas regarding hydrocarbon fluxing and the shallow Ba cycle. Authigenic barite accumulations, either as mounds on the seafloor or as fronts in the sediment, are generally considered to have formed in SO_4^{2-}-rich waters above the SHT (e.g., Brumsack, 1986; Torres et al., 1996a, 2002; Naehr et al., 2000; Dickens, 2001; Greinert et al., 2002; Snyder et al., in press). However, many of the nodules at the mud volcanoes exist below the inferred SHT (Fig. 4), where barite should dissolve. Additionally, the distinct morphologies and barite crystal habits also suggest that rocky and smooth nodules formed by two different processes.

Rocky nodules have three distinguishing characteristics that hint at their genesis. First, the conglomeratic texture of large (~1 cm), poorly supported carbonate clasts suggests fracturing by fluids. Second, the sizable (5 cm) bivalve fragments in some nodules (Fig. 8) indicate that they formed at or near the seafloor. Finally, the infilling of large and common void spaces by anhedral barite crystals (Figs. 7 and 8) suggests that barite rapidly precipitated into pre-existing space.

A specific sequence of processes at mud volcanoes may produce rocky nodules (Fig. 10). Carbonate crusts and bivalve communities often form around active hydrocarbon vents in the GOM (and elsewhere), because the microbial consumption of CH_4 and other hydrocarbons generates consumable biomass and HCO_3^-, which then reacts with seawater Ca^{2+} (Roberts and Aharon, 1994). Periodic eruptions (e.g., Neurauter and Roberts, 1994; MacDonald et al., 2000) would break these crusts and communities, leaving Ba^{2+}-rich vent fluids in the interstices of carbonate fragments. Rapid mixing of these fluids with SO_4^{2-} would precipitate anhedral barite crystals in open pore spaces. After the eruption, mudflows and sedimentation would bury the barite-rich carbonate conglomerates. Once below the SHT, they may begin to dissolve, releasing Ba^{2+} to surrounding pore fluids. Crusts dominated by barite and calcite with minor amounts of kerogen have been documented within 40 cm of the seafloor at nearby mud volcanoes (Fu and Aharon, 1997) (Fig. 3). These crusts have some similarities to the rocky nodules discussed here, although shells and void spaces were not reported. On the basis of sulfur isotopes, barite in these crusts appears to have formed near the seafloor but from microbially modified seawater, where significant SO_4^{2-} had been consumed (Fu and Aharon, 1997). This could also be the case for rocky nodules.

Smooth nodules probably have a different origin, especially considering two additional observations. First, they consist of interlocking barite and carbonate (Figs. 7 and 8), suggesting that the two minerals precipitated contemporaneously. Second, several of the smooth nodules occur within 10 cm of the modern, inferred SHT (Fig. 4).

Smooth nodules may represent lithified horizons where the SHT has remained fixed for extended time (Figs. 2 and 10). Like aerobic oxidation of hydrocarbons, anaerobic oxidation of hydrocarbons removes SO_4^{2-} and produces HCO_3^- (e.g., Borowski et al., 1996). Authigenic barite and carbonate might, therefore, precipitate together at or near the SHT. Under conditions of steady sedimentation, however, the two minerals should have different fates upon passage through the SHT—barite would dissolve while carbonate would remain. As a result, they will not accumulate together in significant concentrations. The coexistence and intermingling of the two minerals within large nodules thus suggest a non-steady state history, where barite and carbonate precipitated at the same depth over a prolonged time interval, presumably because the SHT did not migrate upwards with sedimentation or because sedimentation effectively ceased (Brumsack, 1986; Snyder et al., in press). Potentially, these nodules could signify decreasing hydrocarbon flux after an eruption.

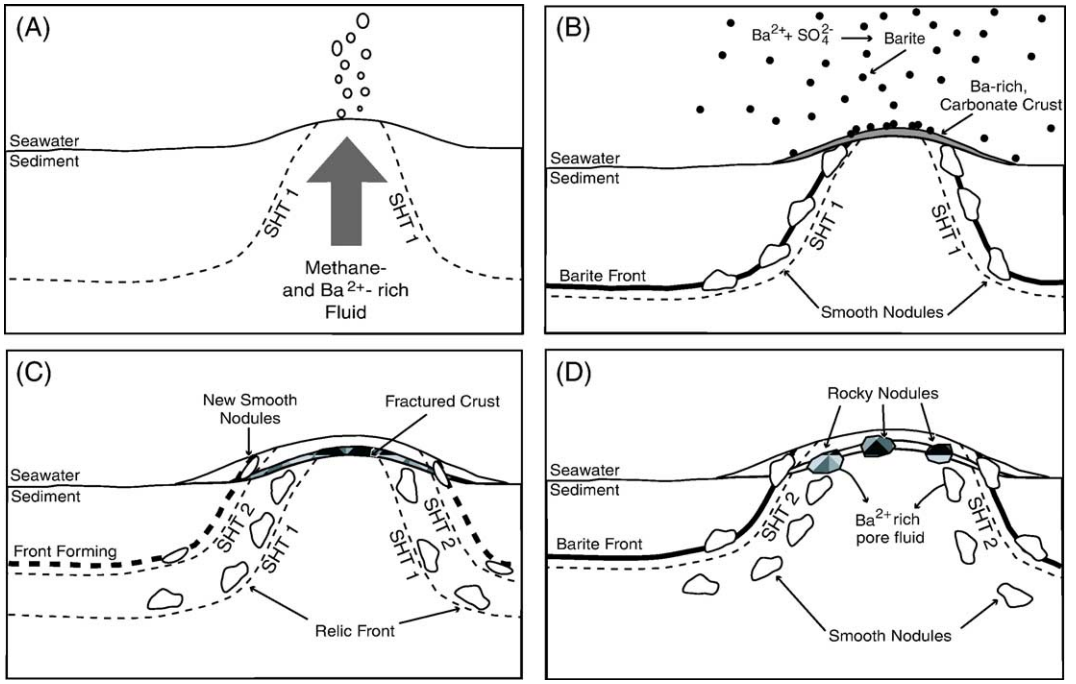

Fig. 10. A model for Ba cycling in high flux environments. (A) Methane- and Ba^{2+}-rich fluids are expelled from the mud volcano into the overlying water column. The SHT is at or near the sediment–water interface and deepens on the flanks of the mud volcano. (B) Dissolved Ba^{2+} rapidly reacts with seawater sulfate, producing small barite crystals that rain-down on the seafloor. A carbonate crust forms above the mud volcano during periods of less violent eruptions. This crust may become Ba-rich as fluids pass through void spaces and crystallize barite. The barite front is established and mimics the modern SHT; smooth nodules form at the barite front. (C) A period of more violent eruptions occurs, producing mudflows on top of fractured carbonate crusts. The SHT migrates upward to accommodate sedimentation. As a result, the old barite front is abandoned, leaving smooth nodules. A barite front begins to form above the new SHT. (D) Fractured carbonate crust is buried as discrete rocky nodules. These nodules and other smooth nodules begin to dissolve because they are below the modern SHT, creating locally elevated dissolved Ba^{2+} concentrations. A new horizon of smooth nodules develops at the barite front.

In cores with multiple smooth nodules (Fig. 4), the SHT has been preserved while new horizons develop. During periods of rapid sedimentation (i.e., mud volcano eruptions), the current SHT is buried and a new SHT is re-established in shallower sediment. Several fronts are observed at once because deeper fronts have not had sufficient time to dissolve completely.

As noted previously, barite crystals found in smooth nodules are either acicular or blocky. Nodules with acicular crystals are typically found near vents whereas blocky crystals typify barite in nodules on the flanks. Because dissolved Ba^{2+} concentrations are greatest proximal to venting, the crystal habit may reflect the amount of dissolved Ba^{2+} during nucleation. Cross-cutting quartz veins are also found in nodules closest to venting. These features may reflect thermal alteration as warm fluids migrate through surrounding sediment.

7.5. Barium expulsion

At both the GB 425 and MC 852/853 study areas, the Ba content of surface sediment appears to form a concentric pattern around the mud volcano (Fig. 5). In the upper 2 cm of sediment, Ba contents exceed 19,000 mg/kg at the center of the mud volcanoes but systematically decrease to less than 40 mg/kg within 683 m down the flanks.

A straightforward mechanism involving periodic fluid eruptions can explain these elevated surficial Ba contents (Fig. 10). As observed in several places (Torres et al., 1996b, 2002; Naehr et al., 2000; Greinert et al., 2002; Aloisi et al., 2004), including the GOM (Fu and Aharon, 1997), fluids charged with hydrocarbons and Ba^{2+} can vent into the overlying water column. The dissolved Ba^{2+} reacts with SO_4^{2-} in seawater to form small, anhedral barite crystals within the water column (Torres et al., 1996b, 2002; Fu and Aharon, 1997). Presumably, these crystals rain down onto the seafloor. Because the fluid is focused at the mud volcano, the barite content of shallow sediment should gradually decrease away from this source.

Excess Ba in surface sediment further distinguishes the Ba cycle at GOM mud volcanoes compared to most previously studied regions. In bathyal settings away

from hydrothermal systems, barite accumulating on the seafloor is often assumed to have arrived by sinking through the water column in association with organic carbon (e.g., Chow and Goldberg, 1960; Dehairs et al., 1980). Indeed, this is the presumed source of barite supplying Ba^{2+} to barite fronts above SHTs elsewhere (Fig. 2). Although some fraction of the overall Ba budget at GOM mud volcanoes may come from "biogenic barite", even the barite in surface sediment may ultimately come from vent fluids.

Most papers regarding the global marine Ba cycle (e.g., Wolgemuth and Broecker, 1970; Paytan and Kastner, 1996) have not considered Ba^{2+} inputs from hydrocarbon vents. The extreme dissolved Ba^{2+} concentrations at mud volcanoes in the GOM and certain other CH_4 charged systems (e.g., the Sea of Okhotsk), along with compelling evidence for periodic discharge of Ba^{2+} to bottom waters, instigate an obvious question (Dickens et al., 2003; Aloisi et al., 2004): do hydrocarbon vents impact regional and global Ba cycling? This study cannot rigorously address the issue because the release of dissolved Ba^{2+} from individual mud volcanoes and other seafloor seep features is undoubtedly variable and episodic, and because the fluid composition of GOM mud volcanoes may not represent hydrocarbon vents in general. Some fraction of dissolved Ba^{2+} added to bottom water also clearly precipitates around the vents (Fig. 5), rather than continuing in aqueous solution. Nonetheless, the upper 3 m of sediment at the MC 852/853 mud volcano holds nominally 10×10^6 mol of dissolved Ba^{2+}, assuming aforementioned parameters, an average dissolved Ba^{2+} concentration of 5000 μM, and a porosity of 70%. Even if all this Ba^{2+} suddenly escaped, it would be a fairly small input compared to approximately $18{,}000 \times 10^6$ mol of Ba^{2+} annually added to the ocean by rivers and hydrothermal activity (Dickens et al., 2003). Thousands of mud volcanoes with elevated dissolved Ba^{2+} would have to steadily discharge to impact the global marine Ba cycle. Interestingly, this may have happened at the Paleocene–Eocene Thermal Maximum (PETM) (Dickens et al., 2003; Svensen et al., 2004).

7.6. Concentric zonation

Detailed work around the Håkon Mosby mud volcano in the North Atlantic shows concentric patterns in various parameters, including pore water chemistry (Milkov et al., 2004). This has led to the suggestion that concentric zonation, presumably driven by central upward fluid migration, may be a common characteristic of mud volcanoes in general (Milkov et al., 2004). Our pore water and sediment chemistry results support this inference. If confirmed elsewhere, this concentric zonation may be an important means of modeling fluid outputs from mud volcanoes.

8. Conclusions

Recent studies have suggested a link between upward fluxing hydrocarbons and Ba cycling in shallow marine sediments (Torres et al., 1996a; Dickens, 2001; Aloisi et al., 2004). In this view, hydrocarbons from below fuel SO_4^{2-} consumption at an SHT, while barite dissolves and precipitates below and above the SHT (Fig. 1). Previous work at mud volcanoes in the GOM has identified barite structures on the seafloor and high dissolved Ba^{2+} concentrations in pore water samples from a few shallow (40 cm) sediment cores (Fu and Aharon, 1998; Aharon et al., 2001), supporting some link between hydrocarbon fluxing and Ba cycling in this region.

In this study, we collected 16 cores across two mud volcanoes in the GOM. Pore waters were extracted and analyzed for salinity, Cl^-, SO_4^{2-}, Ba^{2+}; digested sediments were also analyzed for Ba. Carbonate nodules were extracted from cores and examined for their chemistry, mineralogy and petrography.

In the GOM, the inferred SHT shoals across mud volcanoes, presumably in response to the expulsion of methane and other hydrocarbons. This finding is consistent with limited work in the GOM by previous investigators (Aharon and Fu, 2000, 2003; Joye et al., 2004), and the general observation that hydrocarbon fluxing drives SO_4^{2-} consumption and the depth of the SHT (Borowski et al., 1996, 1999; Hoehler et al., 2000). Further, both dissolved and solid phase Ba data clearly show that the proposed hydrocarbon–SO_4^{2-}–Ba link (Fig. 1) occurs across the inferred SHT. Barium cycling at GOM mud volcanoes is, however, more complicated than that suggested for other regions. Deep formation waters supply Ba^{2+} from below so that most of the Ba does not come from pelagic rain. Even the barite in surface sediment surrounding the mud volcanoes probably comes from below, when periodic fluid venting induces barite precipitation in the water column.

Barium-rich, carbonate nodules are found at both sites and appear to play an important role in Ba cycling. Smooth nodules probably represent lithified barite fronts formed when the SHT remains stationary for extended time, perhaps between episodic pulses in venting. Rocky nodules may form when Ba^{2+}-rich fluids erupt through carbonate crusts that cap mud volcanoes. Upon burial, both types of nodules can release dissolved Ba^{2+} below the SHT, further complicating the shallow Ba cycle.

Acknowledgements

We thank the members and crew of the *R/V Seward Johnson I*, cruise 08/02, particularly Bill Gilhooley; Kathy Schewer and Dave Adamson for their assistance with ion chromatography; Tom Fewless at Rice University for his assistance with the SEM; and Rolf Arvidson at Rice University for his assistance with the XRD. We also thank two anonymous reviewers who offered constructive criticism. This work was funded through the U.S. National Science Foundation (OCE 0117950).

This work was completed while C. Ruppel was on assignment at and wholly supported by the National Science Foundation. The views expressed in this paper are those of the authors and not of the National Science Foundation. **[LW]**

Appendix A. Salinity, major anions and dissolved Ba^{2+} concentrations of pore waters (data presented online)

Sample	Average depth (cm)	Shipboard salinity	Shorebased salinity	Sulfate (mM)	Chloride (mM)	Ba (μM)
GB 425						
GB-GC-7-1	7.5	37	40	28.40	853.6	0.796
GB-GC-7-2	17.5	40	47	1.97	1080.2	8.48
GB-GC-7-3	27.5	47	52	0.41	1197.5	331
GB-GC-7-4	62.5	61	64	0.00	1464.2	2290
GB-GC-7-5	92.5	68	74	0.00	1657.3	3100
GB-PC-11-1	12.5	41	45	0.47	783.7	14.2
GB-PC-11-2	22.5	52	55	1.36	901.1	5.43
GB-PC-11-3	32.5	70	75	0.00	1215.4	1140
GB-PC-11-4	52.5	81	84	0.00	1483.2	1170
GB-PC-11-5	62.5	84	86	0.00	1508.2	1170
GB-PC-11-6	72.5	85	86	0.00	1474.0	1180
GB-PC-11-7	82.5	85	89	0.00	1543.1	1200
GB-PC-11-8	92.5	85	87	0.00	1162.9	1290
GB-PC-11-9	132.5	85	86	0.00	1450.7	1190
GB-PC-12-1	12.5	34	37	7.21	490.6	0.975
GB-PC-12-2	17.5	34	36	7.03	544.2	0.871
GB-PC-12-3	22.5	34	36	6.92	534.3	1.02
GB-PC-12-4	52.5	34	36	5.95	554.4	1.20
GB-PC-12-5	82.5	35	36	4.93	532.0	0.847
GB-PC-12-6	112.5	35	37	3.75	572.1	1.14
GB-PC-12-7	142.5	35	37	2.30	555.9	1.32
GB-PC-12-8	172.5	35	36	2.02	537.4	3.67
GB-PC-12-9	197.5	37	40	0.08	592.0	209
GB-PC-13-1	12.5	35	36	9.42	537.0	0.708
GB-PC-13-2	42.5	35	36	9.21	540.9	0.719
GB-PC-13-3	72.5	35	36	7.95	512.8	0.961
GB-PC-13-4	107.5	35	36	7.20	550.1	0.678
GB-PC-13-5	147.5	35	36	5.30	523.3	0.608
GB-PC-13-6	187.5	33	35	4.65	567.0	0.763
GB-PC-13-7	227.5	33	36	11.29	620.0	0.947
GB-PC-13-8	267.5	33	36	1.84	646.9	20.6

Appendix A (*continued*)

Sample	Average depth (cm)	Shipboard salinity	Shorebased salinity	Sulfate (mM)	Chloride (mM)	Ba (μM)
GB 425						
GB-PC-13-9	293	35	35	0.02	620.2	57.3
GB-PC-14-1	12.5	87	90	0.00	2138.5	7690
GB-PC-14-2	42.5	94	97	0.00	2468.4	7540
GB-PC-14-3	72.5	108	114	0.00	2632.1	4750
GB-PC-14-4	102.5	108	116	0.00	2732.6	4240
GB-PC-14-5	142.5	108	118	0.00	2656.6	3810
GB-PC-14-6	172.5	110	116	0.00	2032.0	3450
GB-PC-14-7	202.5	110	116	0.00	2723.5	2780
GB-PC-14-8	225	108	116	0.00	2710.7	2060
GB-PC-15-1	12.5	35	36	4.89	596.6	1.33
GB-PC-15-2	42.5	38	40	2.47	874.3	8.91
GB-PC-15-3	72.5	44	44	0.43	964.9	544
GB-PC-15-4	102.5	47	46	0.00	1074.5	952
GB-PC-15-5	132.5	55	50	0.00	1156.9	1420
GB-PC-15-6	162.5	64	57	0.00	1318.8	178-
GB-PC-15-7	192.5	65	66	0.00	1620.5	4130
GB-PC-15-8	217.5	73	75	0.07	1793.8	6850
GB-PC-17-1	8.5	57	60	0.00	1378.4	2680
GB-PC-17-2	17.5	60	62	0.00	1423.8	3050
GB-PC-17-3	47.5	71	74	0.00	1748.4	4250
GB-PC-17-4	72.5	77	80	0.00	1848.8	4680
GB-PC-17-5	102.5	79	84	0.09	2011.9	4900
GB-PC-17-6	132.5	81	85	0.00	2044.2	5120
GB-PC-17-7	162.5	82	85	0.00	2056.1	5180
GB-PC-17-8	192.5	84	85	0.18	2005.2	5490
GB-PC-18-1	7.5	34	36	5.70	539.0	0.925
GB-PC-18-2	17.5	34	36	5.27	553.8	1.20
GB-PC-18-3	52.5	35	36	4.51	542.9	1.40
GB-PC-18-4	82.5	35	36	4.06	575.3	2.16
GB-PC-18-5	117.5	34	36	3.52	533.2	1.60
GB-PC-18-6	142.5	34	35	3.24	555.4	2.410
GB-PC-18-7	177.5	34	35	0.80	764.3	27.2
GB-PC-18-8	222.5	35	37	0.00	812.2	644
GB-PC-19-1	12.5	35	36	5.90	533.3	0.849
GB-PC-19-2	22.5	35	36	5.64	560.2	0.515
GB-PC-19-3	52.5	34	35	5.03	525.2	0.664
GB-PC-19-4	92.5	34	35	5.11	570.1	2.14
GB-PC-19-5	132.5	35	35	5.15	535.4	0.703
GB-PC-19-6	172.5	35	36	5.47	531.9	0.526
GB-PC-19-7	212.5	35	35	4.33	546.2	0.539
GB-PC-19-8	252.5	35	35	4.57	564.5	0.597
GB-PC-19-9	292.5	35	36	3.47	540.1	0.623
GB-PC-19-10	322.5	35	35	2.39	566.0	1.20
GB-PC-20-1	12.5	35	36	6.07	670.3	0.947
GB-PC-20-2	22.5	35	37	4.66	573.3	1.24
GB-PC-20-3	52.5	35	37	4.20	573.7	1.16
GB-PC-20-4	92.5	39	41	2.53	662.1	0.973
GB-PC-21-1	12.5	35	37	4.13	533.5	0.556
GB-PC-21-2	22.5	35	37	5.67	569.5	0.590
GB-PC-21-3	57.5	36	38	4.16	551.8	0.567
GB-PC-21-4	87.5	37	39	4.30	579.2	0.675
GB-PC-21-5	127.5	39	40	2.55	572.4	0.799
GB-PC-21-6	167.5	44	46	1.48	774.6	1.37
GB-PC-21-7	217.5	57	61	0.41	1457.0	174
GB-PC-21-8	267.5	66	69	0.56	1667.8	395

(continued on next page)

Appendix A (*continued*)

Sample	Average depth (cm)	Shipboard salinity	Shorebased salinity	Sulfate (mM)	Chloride (mM)	Ba (μM)
GB 425						
GB-PC-21-9	317.5	83	85	0.00	2004.0	677
GB-PC-21-10	357.5	94	98	0.00	2346.5	641
GB-PC-22-1	12.5	36	39	4.56	540.5	0.665
GB-PC-22-2	22.5	36	37	3.70	578.1	0.747
GB-PC-22-3	67.5	39	40	3.68	562.2	0.637
GB-PC-22-4	107.5	40	42	3.59	649.7	0.699
GB-PC-22-5	147.5	44	45	3.22	706.5	1.99
GB-PC-22-6	187.5	48	50	2.41	802.7	0.958
GB-PC-22-7	227.5	62	64	0.00	1281.7	1430
GB-PC-22-8	267.5	69	70	0.00	1395.0	1470
GB-PC-22-9	307.5	75	74	0.00	1542.7	1700
GB-PC-22-10	347.5	93	96	0.00	2056.6	1670
GB-PC-23-1	12.5	36	36	4.36	530.5	0.695
GB-PC-23-2	22.5	36	36	4.73	551.5	0.788
GB-PC-23-3	52.5	35	37	3.51	511.5	0.641
GB-PC-23-4	92.5	36	36	3.15	540.4	0.762
GB-PC-23-5	127.5	37	37	7.64	428.8	2.53
GB-PC-23-6	162.5	37	37	5.84	664.4	1.15
GB-PC-24-1	12.5	37	40	10.47	598.3	0.863
GB-PC-24-2	22.5	37	40	18.03	596.3	0.781
GB-PC-24-3	52.5	37	49	6.57	760.3	2.37
GB-PC-24-4	92.5	61	65	6.26	1167.8	3.99
GB-PC-24-5	132.5	87	90	0.00	1748.5	6360
GB-PC-24-6	192.5	110	116	0.00	2269.5	5920
GB-PC-24-7	232.5	120	128	0.27	2326.8	6050
GB-PC-24-8	282.5	130	134	0.00	2617.1	6090
MC 852/853						
MC-PC-25-1	12.5	71	74	0.00	1324.9	1090
MC-PC-25-2	22.5	81	85	0.00	1716.3	572
MC-PC-25-3	42.5	104	112	0.00	2138.6	2150
MC-PC-25-4	72.5	130	138	0.00	2566.3	3490
MC-PC-25-5	102.5	136	140	0.00	2387.3	3630
MC-PC-25-6	132.5	130	134	0.00	2606.4	1520
MC-PC-25-7	172.5	120	128	0.00	2357.6	581
MC-PC-26-1	12.5	35	40	8.24	579.2	1.34
MC-PC-26-2	22.5	36	39	6.50	501.9	1.23
MC-PC-26-3	62.5	54	56	0.00	1022.3	119
MC-PC-26-4	102.5	66	73	0.00	1375.4	217
MC-PC-26-5	142.5	75	79	0.00	1474.8	268
MC-PC-26-6	182.5	80	83	0.00	1558.6	310
MC-PC-26-7	222.5	86	89	0.00	1666.9	321
MC-PC-26-8	272	88	91	0.00	1747.3	329
MC-PC-26-9	0	34	36	8.27	488.6	0.734
MC-PC-27-1	12.5	35	36	26.14	618.9	0.854
MC-PC-27-2	22.5	30	39	26.18	641.2	1.70
MC-PC-27-3	72.5	31	39	28.82	664.0	1.28
MC-PC-27-4	122.5	31	37	22.68	516.9	1.06
MC-PC-27-5	172.5	30	36	25.65	597.8	1.87
MC-PC-27-6	222.5	32	38	26.91	601.0	2.38
MC-PC-27-7	272.5	32	36	27.71	613.1	0.753
MC-PC-27-8	322.5	30	36	26.40	611.9	1.18
MC-PC-27-9	372.5	35	37	28.23	607.7	0.728
MC-PC-27-10	0	34	39	28.71	650.9	0.534
MC-PC-28-1	12.5	33	36	8.78	539.6	1.27
MC-PC-28-2	22.5	27	36	7.69	549.8	0.862

Appendix A (*continued*)

Sample	Average depth (cm)	Shipboard salinity	Shorebased salinity	Sulfate (mM)	Chloride (mM)	Ba (μM)
MC 852/853						
MC-PC-28-3	52.5	33	38	5.35	425.5	1.12
MC-PC-28-4	82.5	32	36	6.04	525.0	1.22
MC-PC-28-5	112.5	34	38	6.41	549.8	1.93
MC-PC-28-6	157.5	32	36	2.79	398.6	2.45
MC-PC-29-1	12.5	35	36	8.75	534.7	1.24
MC-PC-29-2	22.5	35	36	8.27	528.7	0.781
MC-PC-29-3	62.5	35	38	7.43	585.5	1.16
MC-PC-29-4	102.5	36	38	5.52	529.0	1.41
MC-PC-29-5	152.5	39	40	4.56	574.2	2.49
MC-PC-29-6	192.5	38	39	8.94	666.8	2.63
MC-PC-29-7	232.5	38	40	4.30	758.1	8.15
MC-PC-29-8	272.5	54	40	0.81	714.0	52.1
MC-PC-30-1	12.5	71	96	0.00	1744.7	4020
MC-PC-30-2	22.5	130	128	0.00	2334.8	12100
MC-PC-30-3	72.5	138	140	0.00	2562.9	12100
MC-PC-30-4	112.5	130	140	0.00	2531.3	10100
MC-PC-30-5	192.5	128	142	0.00	2518.2	3640
MC-PC-30-6	257.5	95	102	0.00	1898.8	1420
MC-PC-30-7	267.5	98	104	0.00	1813.1	1040
MC-PC-30-8	277.5	128	134	0.00	2392.6	944
MC-PC-30-9	302.5	130	160	0.00	2168.7	1260

Notes: Sulfate values listed as zero are below the detection limit.

Appendix B. Ba content of extracted sediment and nodules (data presented online)

Core, interval (cm)	Ba (mg/kg)
GB 425	
GB-PC-12, 0–2	1200
GB-PC-12, 30–32	2000
GB-PC-12, 40–42	1130
GB-PC-12, 60–62	182.4
GB-PC-12, 90–92	78.6
GB-PC-12, 100–102	72.6
GB-PC-12, 120–122	71.6
GB-PC-12, 130–132	81.1
GB-PC-12, 150–152	70.9
GB-PC-12, 160–162	75.4
GB-PC-12, 168–170	77.8
GB-PC-12, 180–182	119
GB-PC-12, 184–186	129
GB-PC-12, 188–190	147
GB-PC-12, 192–194	231
GB-PC-13, 0–2	1680
GB-PC-13, 20–22	3950
GB-PC-13, 30–32	8660
GB-PC-13, 32–34CW	14,600
GB-PC-13, 50–52	585
GB-PC-13, 60–62	333
GB-PC-13, 80–82	553
GB-PC-13, 100–102	381
GB-PC-13, 115–117	224
GB-PC-13, 125–127	423

Appendix B (*continued*)

Core, interval (cm)	Ba (mg/kg)
GB 425	
GB-PC-13, 135–137	393
GB-PC-13, 155–157	259
GB-PC-13, 165–167	337
GB-PC-13, 175–177	354
GB-PC-13, 195–197	313
GB-PC-13, 205–207	406
GB-PC-13, 215–217	354
GB-PC-13, 235–237	184
GB-PC-13, 245–247	224
GB-PC-13, 255–257	225
GB-PC-15, 0–2	2360
GB-PC-15, 20–22	3440
GB-PC-15, 30–32	1380
GB-PC-15, 40–42	476
GB-PC-15, 44–46	161
GB-PC-15, 48–50	464
GB-PC-15, 52–54	246
GB-PC-15, 56–58	270
GB-PC-15, 60	624
GB-PC-15, 80–82	638
GB-PC-15, 90–92	619
GB-PC-15, 110–112	388
GB-PC-15, 120–122	345
GB-PC-15, 140–142	491
GB-PC-15, 150–152	1450
GB-PC-15, 170–172	566
GB-PC-15, 180–182	No data
GB-PC-15, 200–202	601
GB-PC-15, 210–212	521
GB-PC-19, 0–2	473
GB-PC-19, 30–32	201
GB-PC-19, 40–42	302
GB-PC-19, 60–62	275
GB-PC-19, 70–72	299
GB-PC-19, 80–82	283
GB-PC-19, 100–102	330
GB-PC-19, 110–112	310
GB-PC-19, 120–122	380
GB-PC-19, 140–142	385
GB-PC-19, 150–152	371
GB-PC-19, 160–162	356
GB-PC-19, 180–182	292
GB-PC-19, 190–192	243
GB-PC-19, 200–202	178
GB-PC-19, 220–222	220
GB-PC-19, 230–232	194
GB-PC-19, 240–242	158
GB-PC-19, 260–262	284
GB-PC-19, 270–272	298
GB-PC-19, 280–282	221
GB-PC-19, 300–302	177
GB-PC-19, 310–312	1070
GB-PC-19, 330–332	204
GB-PC-19, 340–342	No data
GB-PC-19, 344–346	790
GB-PC-19, 348–350	651
GB-PC-19R, 0–2	557
GB-PC-19R, 10–12	512

Appendix B (*continued*)

Core, interval (cm)	Ba (mg/kg)
GB 425	
GB-PC-19R, 20–22	494
GB-PC-19R, 30–32	450
GB-PC-19R, 40–42	277
GB-PC-19R, 50–52	259
GB-PC-19R, 60–62	233
GB-PC-19R, 70–72	250
GB-PC-19R, 80–82	329
GB-PC-19R, 90–92	331
GB-PC-19R, 100–102	327
GB-PC-19R, 110–112	324
GB-PC-19R, 120–122	363
GB-PC-19R, 130–132	385
GB-PC-19R, 140–142	403
GB-PC-19R, 150–152	367
GB-PC-19R, 160–162	357
GB-PC-19R, 170–172	357
GB-PC-19R, 174–176	382
GB-PC-19R, 178–180	333
GB-PC-19R, 182–184	316
GB-PC-19R, 186–188	320
GB-PC-19R, 190–192	318
GB-PC-19R, 194–196	327
GB-PC-19R, 198–200	273
GB-PC-19R, 200–202	234
GB-PC-19R, 204–206	237
GB-PC-19R, 208–210	194
GB-PC-19R, 212–214	205
GB-PC-19R, 216–218	105
GB-PC-19R, 220–222	218
GB-PC-19R, 224–226	243
GB-PC-19R, 228–230	172
GB-PC-19R, 240–242	196
GB-PC-19R, 250–252	78.8
GB-PC-19R, 260–262	68.2
GB-PC-19R, 270–272	72.5
GB-PC-19R, 280–282	No data
GB-PC-19R, 290–292	889
GB-PC-19R, 300–302	552
GB-PC-20, 0–2	273
GB-PC-20, 30–32	183
GB-PC-20, 40–42	369
GB-PC-20, 60–62	1840
GB-PC-20, 70–72	No data
GB-PC-20, 80–82	1050
GB-PC-20, 88–89	463
GB-PC-21, 0–2	1050
GB-PC-21, 30–32	463
GB-PC-21, 40–42	383
GB-PC-21, 60–62	289
GB-PC-21, 70–72	374
GB-PC-21, 90–92	399
GB-PC-21, 100–102	463
GB-PC-21, 110–112	339
GB-PC-21, 130–132	393
GB-PC-21, 140–142	469
GB-PC-21, 190–192	5770
GB-PC-21, 200CW	2300

(continued on next page)

Appendix B (*continued*)

Core, interval (cm)	Ba (mg/kg)
GB 425	
GB-PC-21, 206–208	124
GB-PC-21, 230–232	188
GB-PC-21, 240–242	224
GB-PC-21, 250–252	287
GB-PC-21, 270–272	154
GB-PC-21, 280–282	202
GB-PC-21, 290–292	123
GB-PC-21, 300–302	288
GB-PC-21, 320–322	705
GB-PC-21, 330–332	208
GB-PC-21, 340–342	156
GB-PC-21, 360–362	315
GB-PC-22, 0–2	1060
GB-PC-22, 30–32	555
GB-PC-22, 40–42	440
GB-PC-22, 50–52	362
GB-PC-22, 70–72	420
GB-PC-22, 80–82	420
GB-PC-22, 90–92	358
GB-PC-22, 90–92	430
GB-PC-22, 110–112	271
GB-PC-22, 120–122	256
GB-PC-22, 130–132	266
GB-PC-22, 150–152	468
GB-PC-22, 160–162	479
GB-PC-22, 170–172	583
GB-PC-22, 178–180	1190
GB-PC-22, 190–192	12,900
GB-PC-22, 196–198	2500
GB-PC-22, 198–200	7910
GB-PC-22, 198–200CW	21,100
GB-PC-22, 202–204	427
GB-PC-22, 206–208	505
GB-PC-22, 210–212	241
GB-PC-22, 214–216	907
GB-PC-22, 218–220	262
GB-PC-22, 230–232	773
GB-PC-22, 240–242	596
GB-PC-22, 250–252	397
GB-PC-22, 270–272	388
GB-PC-22, 280–282	344
GB-PC-22, 290–292	366
GB-PC-22, 310–312	537
GB-PC-22, 320–322	351
GB-PC-22, 330–332	130
GB-PC-22, 350–352	284
GB-PC-24, 0–2	6840
GB-PC-24, 30–32	No data
GB-PC-24, 40–42	3360
GB-PC-24, 60–62	1060
GB-PC-24, 70–72	1910
GB-PC-24, 80–82	98.2
GB-PC-24, 85–88CW	726
GB-PC-24, 88–90	381
GB-PC-24, 100–102	2810
GB-PC-24, 104–106	7530
GB-PC-24, 108–110	2590
GB-PC-24, 112–114	2730

Appendix B (*continued*)

Core, interval (cm)	Ba (mg/kg)
GB 425	
GB-PC-24, 116–118	2670
GB-PC-24, 120–122	2700
GB-PC-24, 124–126	3970
GB-PC-24, 128–130	4110
GB-PC-24, 140–142	5220
GB-PC-24, 150–152	7770
GB-PC-24, 160–162	4960
GB-PC-24, 170–172	7840
GB-PC-24, 180–182	7750
GB-PC-24, 198–180CW	13,500
GB-PC-24, 200–202	10,900
GB-PC-24, 209–212CW	10,000
GB-PC-24, 210–212	7870
GB-PC-24, 220–222	7350
GB-PC-24, 240–242	7870
GB-PC-24, 250–252	5620
GB-PC-24, 260–262	8530
GB-PC-24, 270–272	10,900
MC 852/853	
MC-PC-25, 0–2	13,800
MC-PC-25, 4–6	14,700
MC-PC-25, 8–10	13,300
MC-PC-25, 30–32	2370
MC-PC-25, 50–52	1460
MC-PC-25, 60–62	970
MC-PC-25, 80–82	1000
MC-PC-25, 90–92	766
MC-PC-25, 110–112	706
MC-PC-25, 120–122	4740
MC-PC-25, 125–128CW	4660
MC-PC-25, 140–142	2960
MC-PC-25, 150–152	2140
MC-PC-25, 160–162	524
MC-PC-26, 0–2	6360
MC-PC-26, 30–32	1750
MC-PC-26, 34–36	16,700
MC-PC-26, 42–44	444
MC-PC-26, 46–48	142
MC-PC-26, 54–56	124
MC-PC-26, 58–60	141
MC-PC-26, 70–72	140
MC-PC-26, 80–82	134
MC-PC-26, 110–112	153
MC-PC-26, 130–132	167
MC-PC-26, 150–152	218
MC-PC-26, 160–162	290
MC-PC-26, 170–172	416
MC-PC-26, 190–192	268
MC-PC-26, 200–202	192
MC-PC-26, 210–212	182
MC-PC-26, 220–222	137
MC-PC-26, 240–242	191
MC-PC-27, 0–2	319
MC-PC-27, 30–32	335
MC-PC-27, 40–42	303
MC-PC-27, 50–52	343
MC-PC-27, 60–62	361

(continued on next page)

Appendix B (*continued*)

Core, interval (cm)	Ba (mg/kg)
MC 852/853	
MC-PC-27, 80–82	437
MC-PC-27, 90–92	548
MC-PC-27, 100–102	538
MC-PC-27, 110–112	541
MC-PC-27, 130–132	444
MC-PC-27, 140–142	290
MC-PC-27, 150–152	183
MC-PC-27, 160–162	230
MC-PC-27, 180–182	565
MC-PC-27, 190–192	217
MC-PC-27, 200–202	180
MC-PC-27, 210–212	133
MC-PC-27, 230–232	148
MC-PC-27, 240–242	154
MC-PC-27, 250–252	167
MC-PC-27, 260–262	490
MC-PC-27, 280–282	142
MC-PC-27, 290–292	134
MC-PC-27, 300–302	143
MC-PC-27, 310–312	139
MC-PC-27, 330–332	148
MC-PC-27, 340–342	144
MC-PC-27, 350–352	151
MC-PC-27, 360–362	141
MC-PC-27, 380–382	154
MC-PC-27, 390–392	149
MC-PC-27, 400–402	215
MC-PC-28, 0–2	818
MC-PC-28, 30–32	279
MC-PC-28, 40–42	337
MC-PC-28, 60–62	396
MC-PC-28, 70–72	383
MC-PC-28, 90–92	418
MC-PC-28, 100–102	227
MC-PC-28, 120–122	558
MC-PC-28, 130–132	434
MC-PC-28, 140–142	590
MC-PC-28, 150–152	223
MC-PC-29, 0–2	1980
MC-PC-29, 30–32	1370
MC-PC-29, 40–42	1560
MC-PC-29, 50–52	1730
MC-PC-29, 70–72	263
MC-PC-29, 70–72	177
MC-PC-29, 80–82	307
MC-PC-29, 90–92	229
MC-PC-29, 110–112	287
MC-PC-29, 120–122	167
MC-PC-29, 130–132	157
MC-PC-29, 140–142	180
MC-PC-29, 160–162	143
MC-PC-29, 170–172	201
MC-PC-29, 180–182	197
MC-PC-29, 200–202	200
MC-PC-29, 210–212	380
MC-PC-29, 220–222	488
MC-PC-29, 240–242	434
MC-PC-29, 244–246	10,500

Appendix B (*continued*)

Core, interval (cm)	Ba (mg/kg)
MC 852/853	
MC-PC-29, 248–250	1100
MC-PC-29, 252–254	633
MC-PC-29, 256–258	544
MC-PC-29, 260–262	306
MC-PC-29, 264–266	368
MC-PC-29, 268–270	No data
MC-PC-30, 0–2	19,600
MC-PC-30, 4–6	15,200
MC-PC-30, 8–10	13,300
MC-PC-30, 30–32	1730
MC-PC-30, 40–42	1220
MC-PC-30, 50–52	1930
MC-PC-30, 60–62	2220
MC-PC-30, 80–82	2110
MC-PC-30, 90–92	1450
MC-PC-30, 100–102	2690
MC-PC-30, 110–112	1540
MC-PC-30, 140–142	3540
MC-PC-30, 150–152	12,600
MC-PC-30, 153–155	23,300
MC-PC-30, 160–162	10,200
MC-PC-30, 170–172	10,700
MC-PC-30, 180–182	13,200
MC-PC-30, 180–182CW	15,900
MC-PC-30, 200–202	7320
MC-PC-30, 210–212	16,600
MC-PC-30, 220–222	1230
MC-PC-30, 230–232	1410
MC-PC-30, 240–242	4460
MC-PC-30, 258–260CW	13,000
MC-PC-30, 280–282	793
MC-PC-30, 290–292	287
MC-PC-30, 310–312	758
MC-PC-30, 320–322	481.5
MC-PC-30, 330–332	355
MC-PC-30, 340–342	3430
MC-PC-30, 343–345CW	5530
Nodules	
G-13N1	17,300
G-21N1	3400
G-21N2	459
G-22N1	14,900
G-24N1	13,700
G-24N2	23,500
G-24N3	12,800
M-25N1	11,100
M-30N1	17,100
M-30N2a	17,300
M-30N2b	20,700
M-30N3	24,300

Notes: CW denotes sediment that coated carbonate nodules when removed. The sediment was washed off with deionized water and analyzed according to the procedures for sediment samples described above.

References

Aharon, P., Fu, B., 2000. Microbial sulfate reduction rates and sulfur and oxygen isotope fractionations at oil and gas seeps in deep-water Gulf of Mexico. Geochim. Cosmochim. Acta 64, 233–246.

Aharon, P., Fu, B., 2003. Sulfur and oxygen isotopes of coeval sulfate–sulfide in pore fluids of cold seep sediments with sharp redox gradients. Chem. Geol. 195, 201–218.

Aharon, P., Van Gent, D., Fu, B., Scott, L.M., 2001. Fate and effects of barium and radium-rich fluid emissions from hydrocarbon seeps on the benthic habitats of the Gulf of Mexico offshore Louisiana. OCS Study MMS 2001–004, U.S. Department of the Interior, Minerals Management Service, Gulf of Mexico OCS Region, New Orleans.

Aloisi, G., Wallmann, K., Bollwerk, S.M., Derkachev, A., Bohrmann, G., Suess, E., 2004. The effect of dissolved barium on biogeochemical processes at cold seeps. Geochim. Cosmochim. Acta 68, 1735–1748.

Anderson, A.L., Bryant, W.R., 1990. Gassy sediment occurrence and properties; northern Gulf of Mexico. Geo Mar. Lett. 10, 209–220.

Boetius, A., Ravenschlag, K., Schubert, C.J., Rickert, D., Widdel, F., Gieseke, A., et al., 2000. A marine microbial consortium apparently mediating anaerobic oxidation of methane. Nature 407, 623–626.

Borowski, W.S., Paull, C.K., Ussler III, W., 1996. Marine pore-water sulfate profiles indicate in situ methane flux from underlying gas hydrate. Geology 24, 655–658.

Borowski, W.S., Paull, C.K., Ussler III, W., 1999. Global and local variations of interstitial sulfate gradients in deep-water, continental margin sediments: sensitivity to underlying methane and gas hydrates. Mar. Geol. 159, 131–154.

Brooks, J.M., Kennicutt, M.C., Fay, R.R., McDonald, T.J., Sasson, R., 1990. Thermogenic gas hydrates in the Gulf of Mexico. Science 225, 409–411.

Brumsack, H.-J., 1986. The inorganic geochemistry of Cretaceous black shales (DSDP Leg 41) in comparison to modern upwelling sediment from the Gulf of California. In: Summerhayes, C.P., Shackleton, N.J. (Eds.), North Atlantic Palaeoceanography, Geological Society Special Publication, vol. 21, pp. 447–462.

Chow, T.J., Goldberg, E.D., 1960. On the marine geochemistry of barium. Geochim. Cosmochim. Acta 20, 192–198.

Clari, P., Cavagna, S., Martire, L., Hunziker, J., 2004. A Miocene mud volcano and its plumbing system: a chaotic complex revisited (Monferrato, NW Italy). J. Sediment. Res. 74, 662–676.

Dehairs, F., Chesselet, R., Jedwab, J., 1980. Discrete suspended particles of barite and the barium cycle in the ocean. Earth Planet. Sci. Lett. 49, 528–550.

Deigel, F.A., Karlo, J.F., Schuster, D.C., Shoup, R.C., Tauvers, P.R., 1995. Cenozoic structural evolution and tectono-stratigraphic framework of the northern Gulf Coast continental margin. In: Jackson, M.P.A., Roberts, D.G., Snelson, S. (Eds.), Salt Tectonics: A Global Perspective, AAPG Memoir, vol. 65, pp. 109–151.

D'Hondt, S., Rutherford, A., Spivack, A.J., 2002. Metabolic activity of subsurface life in deep-sea sediments. Science 295, 2067–2070.

D'Hondt, S., Jørgensen, B.B., Miller, D.J., Batzke, A., Blake, R., Cragg, B.A., et al., 2004. Distributions of metabolic activities in deep subseafloor sediments. Science 306, 2216–2221.

Dickens, G.R., 2001. Sulfate profiles and barium fronts in sediment on the Blake Ridge: present and past methane fluxes through a large gas hydrate reservoir. Geochim. Cosmochim. Acta 65, 529–543.

Dickens, G.R., 2003. Rethinking the global carbon cycle with a large, dynamic and microbially mediated gas hydrate capacitor. Earth Planet. Sci. Lett. 213, 169–183.

Dickens, G.R., Fewless, T., Thomas, E., Bralower, T.J., 2003. Excess barite accumulation during the Paleocene–Eocene thermal maximum: massive input of dissolved barium from seafloor gas hydrate reservoirs. In: Wing, S.L., Gingerich, P.D., Schmitz, B., Thomas, E. (Eds.), Causes and Consequences of Globally Warm Climates in the Early Paleogene, Special Paper-Geological Society of America, vol. 369, pp. 11–23.

Dimitrov, L.I., 2002. Mud volcanoes—the most important pathway for degassing deeply buried sediments. Earth-Sci. Rev. 59, 49–76.

Eagle, M., Paytan, A., Arrigo, K.R., van Dikjen, G., Murray, R.W., 2003. A comparison between excess barium and barite as indicators of carbon export. Paleoceanography 18, 1021–1052.

Egeberg, P.K., Dickens, G.R., 1999. Thermodynamic and pore water halogen constraints on gas hydrate distribution at ODP site 997 (Blake Ridge). Chem. Geol. 153, 53–79.

Ford, K.H., Naehr, T.H., Skilbeck, C.G., the Leg 201 Scientific Party, 2003. The use of infrared thermal imaging to identify gas hydrate in sediment cores. In: D'Hondt, S.L., Jørgensen, B.B., Miller, D.J. et al. (Eds.), Proc. ODP, Init. Repts, vol. 201. College Station, TX, pp. 201, 1–20.

Formolo, M.J., Lyons, T.W., Zhang, C.L., Kelley, C., Sassen, R., Horita, J., et al., 2004. Quantifying carbon sources in the formation of authigenic carbonates at gas hydrate sites in the Gulf of Mexico. Chem. Geol. 205, 253–264.

Froelich, P.N., Klinkhammer, G.P., Bender, M.L., Luedtke, N.A., Heath, G.R., Cullen, D., et al., 1979. Early oxidation of organic matter in pelagic sediments of the eastern equatorial Atlantic: suboxic diagenesis. Geochim. Cosmochim. Acta 42, 1075–1090.

Fu, B., Aharon, P., 1997. Origin and depositional model of barite deposits associated with hydrocarbon seeps on the Gulf of Mexico slope, offshore Louisiana. Trans.-Gulf Coast Assoc. Geol. Soc. 147, 13–20.

Fu, B., Aharon, P., 1998. Sources of hydrocarbon-rich fluids advecting on the seafloor in the northern Gulf of Mexico. Trans.-Gulf Coast Assoc. Geol. Soc. 48, 73–81.

Fu, B., Aharon, P., Byerly, G.R., Roberts, H.H., 1994. Barite chimneys on the Gulf of Mexico slope: initial report on their petrography and geochemistry. Geo Mar. Lett. 14, 81–87.

Ganesham, R.S., Francois, R., Commeau, J., Brown-Leger, S.L., 2003. An experimental investigation of barite formation in seawater. Geochim. Cosmochim. Acta 67, 2599–2605.

Greinert, J., Boolwerk, S.M., Derkachev, A., Bohrmann, G., Suess, E., 2002. Massive barite deposits and carbonate mineralization in the Derugin Basin, Sea of Okhotak: precipitation processes at cold seep sites. Earth Planet. Sci. Lett. 203, 165–180.

Haese, R.R., Meile, C., Van Cappellen, P., De Lange, G.J., 2003. Carbon geochemistry of cold seeps: methane fluxes and transformation in sediments from Kazan mud volcano, eastern Mediterranean Sea. Earth Planet. Sci. Lett. 212, 361–375.

Hesse, R., Harrison, W., 1981. Gas hydrates (clathrates) causing pore-water freshening and oxygen isotope fractionation in deep-water sedimentary sections of terrigenous continental margins. Earth Planet. Sci. Lett. 55, 453–462.

Hoehler, T.M., Borowski, W.S., Alperin, M.J., Rodriguez, N.M., Paull, C.K., 2000. Model, stable isotope, and radiotracer characterization of anaerobic methane oxidation in gas hydrate-bearing sediments of the Blake Ridge In: Paull, C.K., Matsumoto, R., Wallace, P.J., Dillon, W.P. (Eds.), Proc. ODP, Sci. Results, vol. 164. Ocean Drilling Program, College Station, TX, pp. 79–85.

Jackson, M.P.A., Vendeville, B.C., Schultz-Ela, D.D., 1994. Structural dynamics of salt systems. Annu. Rev. Earth Planet. Sci. 22, 93–117.

Joye, S.B., Boetius, A., Orcutt, B.N., Montaya, J.P., Schluz, H.N., Erickson, M.J., et al., 2004. The anaerobic oxidation of methane and sulfate reduction in sediments from Gulf of Mexico cold seeps. Chem. Geol. 205, 219–238.

Kasten, S., Zabel, M., Heuer, V., Hensen, C., 2004. Processes and signals of non-steady-state diagenesis in deep-sea sediments and their pore waters. In: Wefer, G., Mulitza, S., Ratmeyer, V. (Eds.), The South Atlantic in the Late Quaternary: Reconstruction of Material Budgets and Current Systems. Springer, New York, pp. 431–459.

Kharaka, Y.K., Maest, A.S., Carothers, W.W., Law, L.M., Lamothe, P.J., 1987. Geochemistry of metal-rich brines from central Mississippi Salt Dome basin, USA. Appl. Geochem. 2, 543–561.

Kohl, B., Roberts, H.H., 1994. Fossil foraminifera from four active mud volcanoes in the Gulf of Mexico. Geo Mar. Lett. 14, 126–134.

Lands, L.S., Macpherson, G.L., 1992. Origin of saline formation waters, Cenozoic Section, Gulf of Mexico sedimentary Basin. Am. Assoc. Pet. Geol. Bull. 76, 1344–1362.

MacDonald, I.R., Buthman, D.B., Sager, W.W., Peccini, M.B., Guinasso Jr., N.L., 2000. Pulsed oil discharge from a mud volcano. Geology 28, 907–910.

Macpherson, G.L., 1989. Lithium, boron and barium in formation waters and sediments, northwestern Gulf of Mexico Sedimentary Basin. Ph.D. dissertation, University of Texas, Austin. 286 pp.

Manheim, F.T., Bischoff, J.L., 1969. Geochemistry of pore waters from Shell Oil Company drill holes on the continental slope of the northern Gulf of Mexico. Chem. Geol. 4, 63–82.

McBride, B.C., 1998. The evolution of allochthonous salt along a megaregional profile across the northern Gulf of Mexico basin. AAPG Bull. 82, 1037–1054.

Milkov, A.V., 2000. Worldwide distribution of submarine mud volcanoes and associated gas hydrates. Mar. Geol. 167, 29–42.

Milkov, A.V., Sassen, R., 2002. Thickness of gas hydrate stability zone, Gulf of Mexico continental slope. Mar. Pet. Geol. 17, 981–991.

Milkov, A.V., Vogt, P.R., Crane, K., Lein, A.Y., Sassen, R., Cherkashev, G.A., 2004. Geological, geochemical, and microbial processes at the hydrate-bearing Hakon Mosby mud volcano: a review. Chem. Geol. 205, 219–238.

Naehr, T.H., Stakes, D.S., Moore, W.S., 2000. Mass wasting, ephemeral fluid flow, and barite deposition on the California continental margin. Geology 28, 315–318.

Neurauter, T.W., Bryant, W.R., 1990. Seismic expression of sedimentary volcanism on the continental slope, northern Gulf of Mexico. Geo Mar. Lett. 10, 225–231.

Neurauter, T.W., Roberts, H.H., 1994. Three generations of mud volcanoes on the Louisiana continental slope. Geo Mar. Lett. 14, 120–125.

O'Brien, G.D., 1968. Survey of diapers and diapirism. In: Braunstein, J., O'Brien, G.D. (Eds.), Diapirism and Diapirs, AAPG Memoir, vol. 8, pp. 1–9.

Paytan, A., Kastner, M., 1996. Benthic Ba fluxes in the central equatorial Pacific, implications for the oceanic Ba cycle. Earth Planet. Sci. Lett. 142, 439–450.

Paytan, A., Kastner, M., Campbell, D., Thiemens, M.H., 1993. Sulfur isotopic composition of Cenozoic seawater sulfate. Science 282, 1459–1462.

Peel, F.J., Travis, C.J., Hossack, J.R., 1995. Genetic structural provinces and salt tectonics of the Cenozoic offshore U.S. Gulf of Mexico: a preliminary analysis. In: Jackson, M.P.A., Roberts, D.G., Snelson, S. (Eds.), Salt Tectonics: A Global Perspective, SSPG Memoir, vol. 65, pp. 153–175.

Pfeifer, K., Kasten, S., Hensen, C., Schluz, H.D., 2001. Reconstruction of primary productivity from the barium contents in surface sediments of the South Atlantic Ocean. Mar. Geol. 177, 13–24.

Quinby-Hunt, M.S., Turekian, K.K., 1983. Distribution of elements in sea water. Earth Ocean Sci. 64, 130–132.

Reeburgh, W.S., 1967. An improved interstitial water sampler. Limnol. Oceanogr. 12, 163–165.

Reeburgh, W.S., 1976. Methane consumption in Cariaco Trench waters and sediments. Earth Planet. Sci. Lett. 28, 337–344.

Reitsema, R.H., Lindberg, F.A., Kaltenback, A.J., 1978. Light hydrocarbons in Gulf of Mexico water: sources and relation to structural highs. J. Geochem. Explor. 10, 139–151.

Revil, A., Cathles, L.M., 2002. Fluid transport by solitary waves along growing faults: a field example from the South Eugene Island Basin, Gulf of Mexico. Earth Planet. Sci. Lett. 202, 321–335.

Roberts, H.H., Aharon, P., 1994. Hydrocarbon-derived carbonate buildups of the northern Gulf of Mexico continental slope: a review of submersible investigations. Geo Mar. Lett. 14, 135–148.

Roberts, S.J., Nunn, J.A., 1995. Episodic fluid expulsion from geopressured sediments. Mar. Pet. Geol. 12, 195–204.

Roberts, H.H., Aharon, P., Carney, R., Larkin, J., Sassen, R., 1990. Sea floor responses to hydrocaron seeps, Louisiana continental slope. Geo Mar. Lett. 10, 232–243.

Rowan, M.G., Jackson, M.P.A., Trudgill, B.D., 1999. Salt-related fault families and fault welds in the northern Gulf of Mexico. AAPG Bull. 83, 1454–1484.

Ruppel, C., Dickens, G.R., Castellini, D.G., Gilhooly, W., Lizarralde, D., 2005. Heat and salt in gas hydrate formation in the northern Gulf of Mexico. Geophys. Res. Lett. 32, LO4605.

Rutten, A., de Lange, G.J., 2002. A novel selective extraction of barite, and its applications to eastern Mediterranean sediments. Earth Planet. Sci. Lett. 198, 11–24.

Sager, W.W., Lee, C.S., MacDonald, I.R., Schroeder, W.W., 1999. High-frequency near-bottom acoustic reflection signature of hydrocarbon seeps on the northern Gulf of Mexico continental slope. Geo Mar. Lett. 18, 267–276.

Sassen, R., Milkov, A.V., Roberts, H.H., Sweet, S.T., DeFreitas, D.A., 2003. Geochemical evidence of rapid hydrocarbon venting from a seafloor-piercing mud diapir, Gulf of Mexico continental shelf. Mar. Geol. 198, 319–329.

Seewald, J.S., 2003. Organic–inorganic interactions in petroleum-producing sedimentary basins. Nature 426, 327–333.

Snyder, G.T., Dickens, G.R., Castellini, D.G., in press. Labile barite contents and dissolved barium concentrations on Blake Ridge: new perspectives on barium cycling above gas hydrate systems. J. Geochem. Explor.

Suess, E., Torres, M.E., Bohrmann, G., Collier, R.W., Greinert, J., Linke, P., et al., 1999. Gas hydrate destabilization: enhanced dewatering, benthic material turnover and large methane plumes at the Cascadia convergent margin. Earth Planet. Sci. Lett. 170, 1–15.

Svensen, H., Planks, S., Malthe-Sørenssen, A., Jamtveit, B., Myklebust, R., Eidem, T.R., et al., 2004. Release of methane from a volcanic basin as a mechanism for initial Eocene global warming. Nature 429, 542–545.

Thomas, R.D., 2003. 3-D multichannel seismic reflection study of variable flux hydrocarbon seeps, continental slope, northern Gulf

of Mexico. M.S. thesis, Texas A&M University, College Station. 57 pp.
Tissot, B.P., Welte, D.H., 1984. Petroleum Formation and Occurrence. Springer Verlag, New York. 699 pp.
Torres, M.E., Brumsack, H.-J., Bohrmann, G., Emeis, K.C., 1996a. Barite fronts in continental margin sediments: a new look at barium remobilization in the zone of sulfate reduction and formation of heavy barites in diagenetic fronts. Chem. Geol. 127, 125–139.
Torres, M.E., Bohrmann, G., Suess, E., 1996b. Authigenic barites and fluxes of barium associated with fluid seeps in the Peru subduction zone. Earth Planet. Sci. Lett. 144, 469–481.
Torres, M.E., McManus, J., Huh, C.A., 2002. Fluid seepage along the San Clemente Fault scarp: basin-wide impact on barium cycling. Earth Planet. Sci. Lett. 203, 181–194.
Torres, M.E., Bohrmann, G., Dubé, T.E., Poole, F.G., 2003. Formation of modern and Paleozoic stratiform barite at cold methane seeps on continental margins. Geology 31, 897–900.
Tsunogai, U., Yoshida, N., Gamo, T., 2002. Carbon isotopic evidence of methane oxidation through sulfate reduction in sediment beneath cold seep vents on the seafloor at Nankai Trough. Mar. Geol. 187, 145–160.
Wolgemuth, K., Broecker, W., 1970. Barium in sea water. Earth Planet. Sci. Lett. 8, 372–378.
Worrall, D.M., Snelson, S., 1989. Evolution of the northern Gulf of Mexico, with emphasis on Cenozoic growth faulting and the role of salt. In: Bally, A.W., Palmer, A.R. (Eds.), The Geology of North American—An Overview. The Geological Society of America, Boulder, pp. 97–138.